Available online at www.sciencedirect.com
ScienceDirect
International Journal of Heat and Fluid Flow 29 (2008) 387–414
International Journal of HEAT AND FLUID FLOW
www.elsevier.com/locate/ijhff

Experimental and numerical investigation of turbulent cross-flow in a staggered tube bundle

S.S. Paul, S.J. Ormiston *, M.F. Tachie

Department of Mechanical and Manufacturing Engineering, University of Manitoba, Winnipeg, MB, Canada R3T 5V6

Received 13 September 2006; received in revised form 3 October 2007; accepted 18 October 2007
Available online 11 December 2007

Abstract

This paper presents the results of measurements and numerical predictions of turbulent cross-flow in a staggered tube bundle. The bundle consists of transverse and longitudinal pitch-to-diameter ratios of 3.8 and 2.1, respectively. The experiments were conducted using a particle image velocimetry technique, in a flow of water in a channel at a Reynolds number of 9300 based on the inlet velocity and the tube diameter. A commercial CFD code, ANSYS CFX V10.0, is used to predict the turbulent flow in the bundle. The steady and isothermal Reynolds–Averaged Navier–Stokes (RANS) equations were used to predict the turbulent flow using each of the following four turbulence models: a k-epsilon, a standard k-omega, a k-omega-based shear stress transport, and an epsilon-based second moment closure. The epsilon-based models used a scalable wall function and the omega-based models used a wall treatment that switches automatically between low-Reynolds and standard wall function formulations.

The experimental results revealed extremely high levels of turbulence production by the normal stresses, as well as regions of negative turbulence production. The convective transport by mean flow and turbulent diffusion were observed to be significantly higher than in classical turbulent boundary layers. As a result, turbulence production is generally not in equilibrium with its dissipation rate. In spite of these characteristics, it was observed that the Reynolds normal stresses approximated from the k-based two-equation models were in a closer agreement with experiments than values obtained from the second moment closure. The results show that none of the turbulence models was able to consistently reproduce the mean and turbulent quantities reasonably well. The omega-based models predicted the mean velocities better in the developing region while the epsilon-based models gave better results in the region where the flow is becoming spatially periodic.

Keywords: PIV; RANS; Turbulent flow; Tube bundle; Turbulence model

1. Introduction

Cross-flow in tube bundles has wide practical applications in the design of heat exchangers, in flow across overhead cables, and in cooling systems for nuclear power plants. For these reasons, numerous measurements of turbulent cross-flow in tube bundles have been made to advance a physical understanding of such flows. Correlations have also been developed for predicting pressure drop and heat transfer parameters in cross-flow in tube bundles. Balabani (1996) and Paul et al. (2007) presented comprehensive reviews of earlier relevant studies which are not repeated here. The literature reveals that extensive measurements of the mean velocities and Reynolds stresses have been made using hot-wire, LDA and PIV methods. Measurements of the triple correlations and the various terms in transport equations for the turbulent kinetic energy and Reynolds stresses, however, have not yet been reported.

The ability to correctly predict complex turbulent flows is fundamental to the design of many fluid engineering systems. Considerable efforts have been made in the development of turbulence models of varying complexity. Hwang and Jaw (1998), Hanjalic (1994), Gatski and Rumsey (2002) and Leschziner (2006), for example, presented discussion on various aspects of turbulence modeling and

* Corresponding author. Tel.: +1 204 474 8639; fax: +1 204 275 7507.
E-mail address: sormist@cc.umanitoba.ca (S.J. Ormiston).

0142-727X/$ - see front matter © 2007 Elsevier Inc. All rights reserved.
doi:10.1016/j.ijheatfluidflow.2007.10.001

Nomenclature

C_k	convection term in the turbulent kinetic energy budget [$m^2 s^{-3}$]
d	tube diameter [m]
D_k	viscous diffusion term in the turbulent kinetic energy budget [$m^2 s^{-3}$]
k	turbulent kinetic energy [$m^2 s^{-2}$]
L_{ds}	downstream length (Fig. 4a) [m]
l_r	recirculation length [m]
L_{us}	upstream length (Fig. 4a) [m]
Nx	number of grid points in x-direction
Ny	number of grid points in y-direction
P	pressure [$N m^{-2}$]
P_k	production term in the turbulent kinetic energy budget [$m^2 s^{-3}$]
r_x	x-direction geometric grid expansion and contraction factor
r_y	y-direction geometric grid expansion and contraction factor
Re_∞	Reynolds number based on the inlet velocity ($=U_\infty d/\nu$)
S_L	longitudinal pitch [m]
S_L^*	longitudinal pitch-to-diameter ratio ($=S_L/d$)
S_T	transverse pitch [m]
S_T^*	transverse pitch-to-diameter ratio ($=S_T/d$)
U	x-direction mean velocity component [$m s^{-1}$]
U_∞	approach velocity [$m s^{-1}$]
u_τ	friction velocity ($=(\tau_w/\rho)^{0.5}$) [$m s^{-1}$]
u'	x-direction velocity fluctuation [$m s^{-1}$]
u^2	Reynolds normal stress along the x-axis [$m^2 s^{-2}$]
$-uv$	Reynolds shear stress [$m^2 s^{-2}$]
u^3, v^3, u^2v, uv^2	triple correlations of fluctuating velocity components [$m^3 s^{-3}$]
V	y-direction mean velocity component [$m s^{-1}$]
v'	y-direction velocity fluctuation [$m s^{-1}$]
v^2	Reynolds normal stress along the y-axis [$m^2 s^{-2}$]
W	z-direction mean velocity component [$m s^{-1}$]
w'	z-direction velocity fluctuation [$m s^{-1}$]
x	streamwise coordinate [m]
y	transverse coordinate [m]
y^+	non-dimensional distance from the wall ($=\Delta y u_\tau/\nu$)
Δy	first grid spacing near a wall [m]
z	span-wise coordinate [m]

Greek symbols

ε	turbulent dissipation rate [$m^2 s^{-3}$]
ε_k	dissipation term in the turbulent kinetic energy budget [$m^2 s^{-3}$]
μ	fluid dynamic viscosity [$N s m^{-2}$]
μ_t	turbulent eddy viscosity [$N s m^{-2}$]
ν	kinematic viscosity [$m^2 s^{-1}$]
Π_k	convective diffusion term in the turbulent kinetic energy budget [$m^2 s^{-3}$]
ρ	fluid density [$kg m^{-3}$]
τ_w	wall shear stress [$N m^{-2}$]
η	Kolmogorov length scale [μm]
ω	specific dissipation rate [s^{-1}]

Acronyms

2D	two-dimensional
3D	three-dimensional
CFD	computational fluid dynamics
DNS	direct numerical simulation
LDA	laser Doppler anemometry
LES	large eddy simulation
LRR-IP	Launder, Reece and Rodi isotropisation of production
PIV	particle image velocimetry
SGS	sub-grid-scale
SST	shear stress transport

their applications. The sophistication of turbulence models can vary from the simple algebraic models (e.g. mixing length models), through two-equation eddy-viscosity models, to second moment closures, which solve transport equations for the Reynolds stresses. Detailed descriptions of the various turbulence models can be found in Hanjalic (1994) and Pope (2000).

The prediction of turbulent cross-flow in a tube bundle was the subject of an international symposium on turbulence modeling (Leschziner and Launder, 1993). It is recognized, however, that this flow still poses a challenge to turbulence modeling (Hanjalic, 1994). Several fluid flow and heat transfer simulations in tube bundles which focus on turbulent flows have been reported. Table 1 summarizes some of the pertinent numerical studies of turbulent flow through tube bundles. Simonin and Barcouda (1988) performed experimental and numerical studies of turbulent cross-flow in a tube bundle. The measurements were made using an LDA technique. The transverse and longitudinal pitch-to-diameter ratios, S_T^* and S_L^*, were 2.074 and 1.037, respectively. For the numerical study, they used a k–ε model to predict the mean velocities and turbulent kinetic energy. It was reported that the predicted mean velocities were in good agreement with the measured values. Significant discrepancies exist, however, between the measured and predicted turbulent kinetic energy. Balabani et al. (1994) employed an LDA technique to measure mean velocities and turbulent intensities in a staggered tube bundle. The measured data were compared with the predictions using a standard k–ε turbulence model with and

Table 1
Summary of previous numerical studies

Author(s)	Model(s)	Reynolds number	Data used
Simonin and Barcouda (1988)	k–ε	$Re_\infty = 18{,}000$	Simonin and Barcouda (1988), experimental data
Balabani et al. (1994)	k–ε	$Re_{max} = 12{,}858$	Balabani et al. (1994)
Meyer (1994)	Standard k–ε LRR-IP wall function	$Re_{max} = 32{,}000$	Meyer (1994)
Bouris and Bergeles (1999)	LES- (sub-grid scale)	$Re_{max} = 12{,}858$	Balabani et al. (1994)
Watterson et al. (1999)	Low-Reynolds k–ε	$Re_\infty = 21{,}000$	Simonin and Barcouda (1988), experimental data
Rollet-Miet et al. (1999)	LES-Smagorinsky	$Re_{max} = 40{,}000$	Simonin and Barcouda (1988), experimental data
Benhamadouche and Laurence (2003)	LES and transient RANS	$Re_b = 9000$	Simonin and Barcouda (1988), experimental data
Moulinec et al. (2004)	3-*D DNS*	$Re_\infty = 6000$	Simonin and Barcouda (1988), experimental data
Hassan and Barsamian (2004)	LES -3D	$Re_\infty = 21{,}700$	Simonin and Barcouda (1988), experimental data

All studies except Meyer (1994) used in-house codes; Meyer (1994) used a commercial CFD code. In-house implies that the code was developed as part of the non-commercial research work of the author(s).

without a curvature modification. Bouris and Bergeles (1999) used an LES approach with the Smagorinsky SGS model to predict the experiments of Balabani et al. (1994) In both studies, they obtained good agreement with the experimental results. The mean velocity profile, however, showed slight discrepancy in the flow recirculation regions. Meyer (1994) employed LDA to measure two-dimensional mean velocities and Reynolds stresses in two successive rows in the middle of a tube bundle. The measured values were compared with predictions using both a standard k–ε model and the second moment closure proposed by Launder et al. (1975), termed LRR-IP, with a wall function in its steady formulation. They found that both models were unable to give good predictions of the flow. Numerical predictions of the Simonin and Barcouda experiment in a typical inter-tube region in which spatial periodicity has been established were made by Watterson et al. (1999), Rollet-Miet et al. (1999), Benhamadouche and Laurence (2003) and Hassan and Barsamian (2004). Watterson et al. (1999) used a low-Reynolds number k–ε model. For their comparisons, they modelled flow with a Reynolds number of 21,000 based on the approach velocity. It was reported that the predicted mean values were in good agreement and the Reynolds stresses showed encouraging agreement with the measured values. Rollet-Miet et al. (1999) employed LES and a k–ε model. They reported that the mean velocity profiles were well predicted in the two cases. In the wake region, however, the k–ε model gave poorer prediction of the Reynolds stresses than the LES. Benhamadouche and Laurence (2003) employed LES, coarse LES, and transient Reynolds stress transport models in 2D and 3D, with two levels of grid refinement. For their comparisons, they modeled flow with a Reynolds number of 9000 based on the bulk velocity (based on the inlet volume flow rate and cross-sectional area) and tube diameter. They reported that the LES with the fine mesh are comparable to the experiments. The results from the coarse LES were also in a reasonable agreement with the measured values. Hassan and Barsamian (2004) used LES and observed good agreement with the measured mean flow and Reynolds stresses. Paul et al. (2004) used a low-Reynolds number k–ε model, a k–ω model, and an ε-based second moment closure model to predict flow in the typical section of the experiments of both Simonin and Barcouda (1988) and Balabani (1996). They reported that k–ε and k–ω models give better predictions of the mean flow in a region just before and after a tube than a second moment closure (LRR-IP) model. It is important to note that the second moment closure did not produce consistently good predictions of the Reynolds stresses. Recently, Moulinec et al. (2004) used 3D DNS to predict the experiments of Simonin and Barcouda. The Navier–Stokes equations were discretized on a staggered Cartesian grid with the help of a finite volume approach. For their comparisons, they performed the simulation of the flow with a Reynolds number of 6000 based on the bulk velocity and tube diameter. Overall, they reported that their predictions were in good agreement with those of the experiments. In our previous paper (Paul et al., 2007), we reported comprehensive planar PIV measurements in a staggered tube bundle at three Reynolds numbers. The mean velocities, turbulent intensities, Reynolds stresses and terms in the Reynolds Averaged Navier Stokes equations were presented and discussed in detail.

The first objective of the present study is to perform detailed assessment of the ability of the commercial CFD code, ANSYS CFX, together with four different turbulence models in their steady state formulations, k–ε, k–ω, SST, and LRR-IP, to reproduce the mean flow and turbulent quantities in a staggered tube bundle. As is well known, turbulent flow in tube bundles is generally characterized by significant three-dimensional flow structures and highly fluctuating wake regions with vortex shedding. Consistent with some of the previous studies, however, a two-dimensional steady state simplification has been chosen for the numerical studies. The second objective is to present, for the first time, some of the terms in the transport equations for the turbulent kinetic energy and Reynolds stresses obtained from the PIV measurements to provide insight into turbulence production and transport mechanisms in tube bundles.

2. Experimental set-up and measurement procedure

The set-up and measurement procedure is the same as in Paul et al. (2007), so only a summary is provided here. The experiments were performed in a recirculation type water

tunnel with a test section of 200 mm wide, 200 mm deep and 2500 mm long. A contraction with a six-to-one area ratio and a symmetrical cross-section is used to reduce the turbulence intensity by accelerating the mean flow. The test section was fabricated using clear acrylic to facilitate optical access. Fig. 1a shows a sectional side-view of the tube bundle model used. The bundle consists of 6 rows of tubes of outer diameter of 25.4 mm arranged in staggered array. As shown in the figure, each row has 1 or 2 full tubes. Half tubes were also mounted along the top and bottom walls of the test model alternately to simulate an infinite tube bundle and minimize the wall boundary layer. The transverse and longitudinal pitch-to-diameter ratios, S_T^* and S_L^*, were 3.8 and 2.1, respectively. The length-to-diameter ratio of the rods was 7.5. This is higher than 7.2 used by Balabani et al. (1994), who considered measurements at the mid-span to be free from end effects. Indeed, data presented in Paul et al. (2007) clearly demonstrate that the mean flow is two-dimensional in the mid-plane of the channel. Also shown in Fig. 1 are the key geometrical parameters of the tube bundle model used. The origin of the coordinate system is defined to be at the center of the middle tube in the first row. Here, the streamwise and transverse directions are denoted by x and y, respectively. The z-axis (span-wise), not shown, is assigned to the direction pointing out of the paper. The experiments reported in the present study were performed at a Reynolds number of 9300. This value is based on the tube diameter ($d = 25.4$ mm) and approach velocity in the water tunnel of 0.34 m/s. Fig. 1b shows the details of the region where most results will be presented using spatial coordinates normalized by the tube diameter.

The flow was seeded with polyamide seeding particles having mean diameter of 5 μm and specific gravity of 1.03. A 120 mJ/pulse Nd-YAG laser was used to illuminate the flow field, and the images were acquired using a 2048 pixel × 2048 pixel CCD camera. The acquired images were interrogated using adaptive correlation analyses and a moving average validation scheme. Preliminary measurements were conducted to determine the sample size required to achieve statistically converged results for the mean flow and turbulence statistics. Based on the results, a sample size of 2400 was used to compute those statistics in this work. It should be mentioned that the experimental results presented subsequently were not frequency filtered for the vortex shedding. The majority of the results will be presented at the following x/d locations: 0.85, 1.25, 2.95, 3.35, 5.05, 5.45, 7.15 and 7.55 in the region $0.0 \leqslant y/d \leqslant 3.8$, as indicated in Fig. 1b. Some of the results will be presented at $y/d = 0$ in the region $0.0 \leqslant x/d \leqslant 8.0$, which is also in the region shown in Fig. 1b. The approach velocity, U_∞, will be used to normalize both the mean velocities and the turbulence quantities. As reported in Paul et al. (2007), at $x/d = -10$, it was found that the measured mean

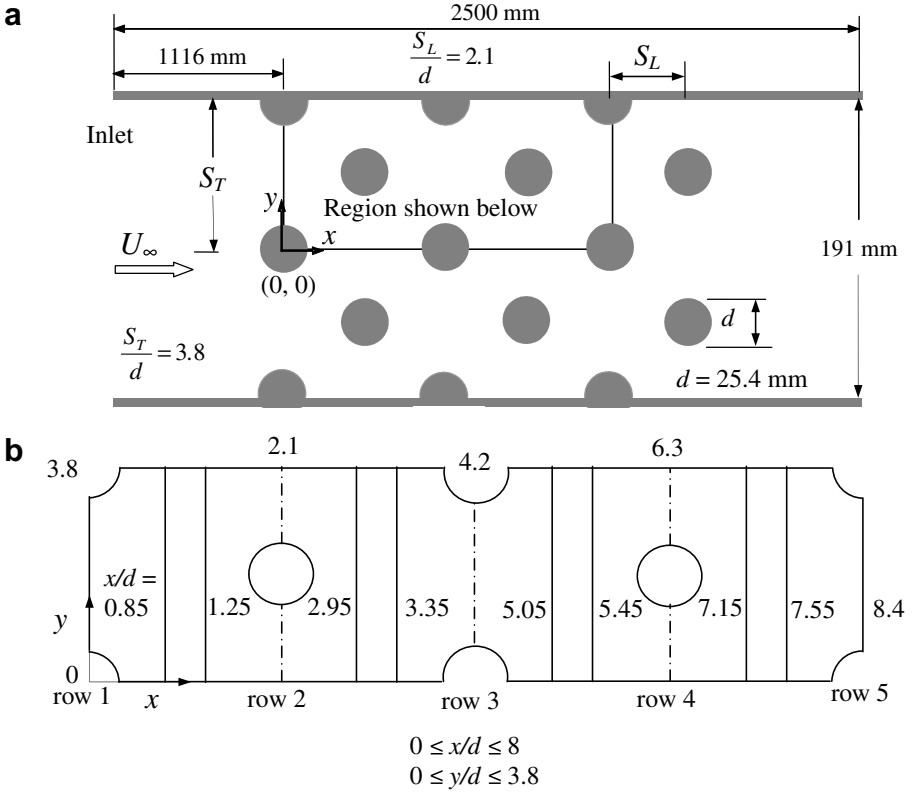

Fig. 1. (a) Cross-sectional view of the tube bundle model with the definition of geometrical parameters and the coordinate system used, and (b) locations at which results are presented: $x/d = 0.85$, 1.25, 2.95, 3.35, 5.05, 5.45, 7.15 and 7.55.

velocity is uniform across the central 70% of the channel with a boundary layer thickness of 34 mm. The streamwise and transverse turbulence intensities in the central portion of the channel were 4% and 3%, respectively. A detailed description of the uncertainty analyses of the present study can be found in Paul et al. (2007). The measurement uncertainty at 95% confidence level in mean velocities, turbulence intensities, and Reynolds stresses are estimated to be ±3%, ±7%, and ±10%, respectively. Close to the tubes, uncertainties in mean velocities and Reynolds stresses are estimated to be ±5% and ±12.5%, respectively. The uncertainties in the first derivatives are of the order of ±15%. When present in some graphs, error bars are used to indicate measurement uncertainty at 95% confidence level.

2.1. Spatial resolution

The influence of spatial resolution on the mean and the fluctuating components in turbulent flows has been studied using PIV by Lecordier et al. (2001) and Fouras and Soria (1998). These studies revealed that when the interrogation area size becomes larger, the PIV tends to underestimate the velocity fluctuations. Saarenrinne and Piirto (2000) and Piirto et al. (2003) employed PIV to estimate the dissipation rate downstream of a backward facing step. They reported that the best estimate for the dissipation rate is achieved when the spatial resolution is close to the Kolmogorov length scale and the velocity measurement error is kept small. They suggested that the spatial distance between the adjacent vectors should be at a distance shorter than the Kolmogorov length scale given by $\eta = (\nu^3/\varepsilon)^{1/4}$, where ν is the kinematic viscosity and ε is the dissipation rate, given by $\varepsilon = A(u^3/L)$, where A is a constant and has a value of order one, u is the turbulence level in the main flow direction, and L is on the order of the integral length scale.

In order to evaluate any effects of spatial resolution on the mean velocities, Reynolds stresses, triple correlations and some of the terms in the transport equation for the turbulent kinetic energy, the acquired images were processed using 32 × 32 pixels and 32 × 16 pixels, both with 50% overlap. The corresponding physical spacing between vectors or data points is, respectively, 1.56 mm × 1.56 mm and 1.56 mm × 0.78 mm. The exact equation for the turbulent kinetic energy, k, can be found in Hinze (1975):

$$\frac{\partial k}{\partial t} = \underbrace{-U_i\frac{\partial k}{\partial x_i}}_{C_k} \underbrace{-\frac{\partial}{\partial x_i}\overline{u_i\left(\frac{p}{\rho}+k\right)}}_{\Pi_k} \underbrace{-\overline{u_iu_j}\frac{\partial U_j}{\partial x_i}}_{P_k} + \underbrace{\nu\frac{\partial}{\partial x_i}\overline{u_j\left(\frac{\partial u_i}{\partial x_j}+\frac{\partial u_j}{\partial x_i}\right)}}_{D_k} \underbrace{-\nu\overline{\left(\frac{\partial u_i}{\partial x_j}+\frac{\partial u_j}{\partial x_i}\right)\frac{\partial u_j}{\partial x_i}}}_{\varepsilon_k} \quad (1)$$

The term on the left side is the time rate of change of kinetic energy, C_k is the convective transport, Π_k is the convective diffusion, P_k is the production, D_k is the viscous diffusion, and ε_k is the viscous dissipation. It should be noted that a planar PIV cannot measure all the components in the various terms in Eq. (1). Therefore, only the components that can be measured directly or approximated from measured values are retained in the production (P_k), dissipation (ε_k) and convective (C_k) terms in Eqs. (2)–(4):

$$P_k = \left(-u^2\frac{\partial U}{\partial x} - v^2\frac{\partial V}{\partial y}\right) - \left(\langle uv\rangle\left(\frac{\partial U}{\partial y}+\frac{\partial V}{\partial x}\right)\right) \quad (2)$$

$$\varepsilon_k = \nu\left[2\overline{\left(\frac{\partial u}{\partial y}\frac{\partial v}{\partial x}\right)} + \overline{\left(\frac{\partial u}{\partial y}\right)^2} + \overline{\left(\frac{\partial v}{\partial x}\right)^2} + 2\overline{\left(\frac{\partial u}{\partial x}\right)^2} + 2\overline{\left(\frac{\partial v}{\partial y}\right)^2} + 2\overline{\left(\frac{\partial w}{\partial z}\right)^2}\right] \quad (3)$$

$$C_k = 0.5\left\{U\left(\frac{\partial}{\partial x}uu + \frac{\partial}{\partial x}vv\right) + V\left(\frac{\partial}{\partial y}uu + \frac{\partial}{\partial y}vv\right)\right\} \quad (4)$$

Eq. (3) is identical to that employed by Piirto et al. (2003) in their PIV study of a backward facing step. Because the spanwise velocity was not measured, the last term in the expression for ε_k was estimated from the continuity equation for the fluctuating velocity components as follows: $\overline{(\partial w/\partial z)^2} = \overline{(\partial u/\partial x + \partial v/\partial y)(\partial u/\partial x + \partial v/\partial y)}$. It is important to note that the first two terms on the right hand side of Eq. (2) consist of the contributions from normal stresses, and the last two consist of the contribution from the shear stress. All velocity derivatives in this study were estimated using a second order central differencing.

Paul et al. (2007) classified this flow into a developing region for $x/d \leqslant 3.35$ and a developed (spatially periodic) region for $x/d \geqslant 5.05$. Therefore, profiles at $x/d = 3.35$ and $x/d = 5.45$ were chosen as typical locations at which to study the effects of spatial resolution. Fig. 2 shows profiles of the streamwise mean velocity, turbulent intensities, Reynolds shear stress, and triple correlations for both interrogation area sizes. The figure reveals that at $x/d = 5.45$, the various profiles collapse reasonably well, except for u^3. It is also observed that the slight variations in the profiles of turbulent intensities (i.e., $1.3 \leqslant y/d \leqslant 2.6$) at $x/d = 3.35$ (Fig. 2b and c), are within measurement error. However, at $x/d = 3.35$ (Fig. 2e), scatter in u^3 precludes any accurate assessment of spatial resolution. It is thought that the scatter might be due to shadows caused by the difference in refractive index between the acrylic tubes and the water. Overall, the results imply that there is no significant effect of spatial resolution in regions where significant shadows were not present.

Fig. 3 shows profiles of the production, dissipation, and convection terms in the turbulent kinetic energy budget. All terms are non-dimensionalized by U_∞^3/d. Fig. 3a and c reveal that at $x/d = 5.45$, the profiles of the production and convection terms show no significant effects of spatial resolution. However, slight variation is observed in the profiles of the production term in the recirculation region

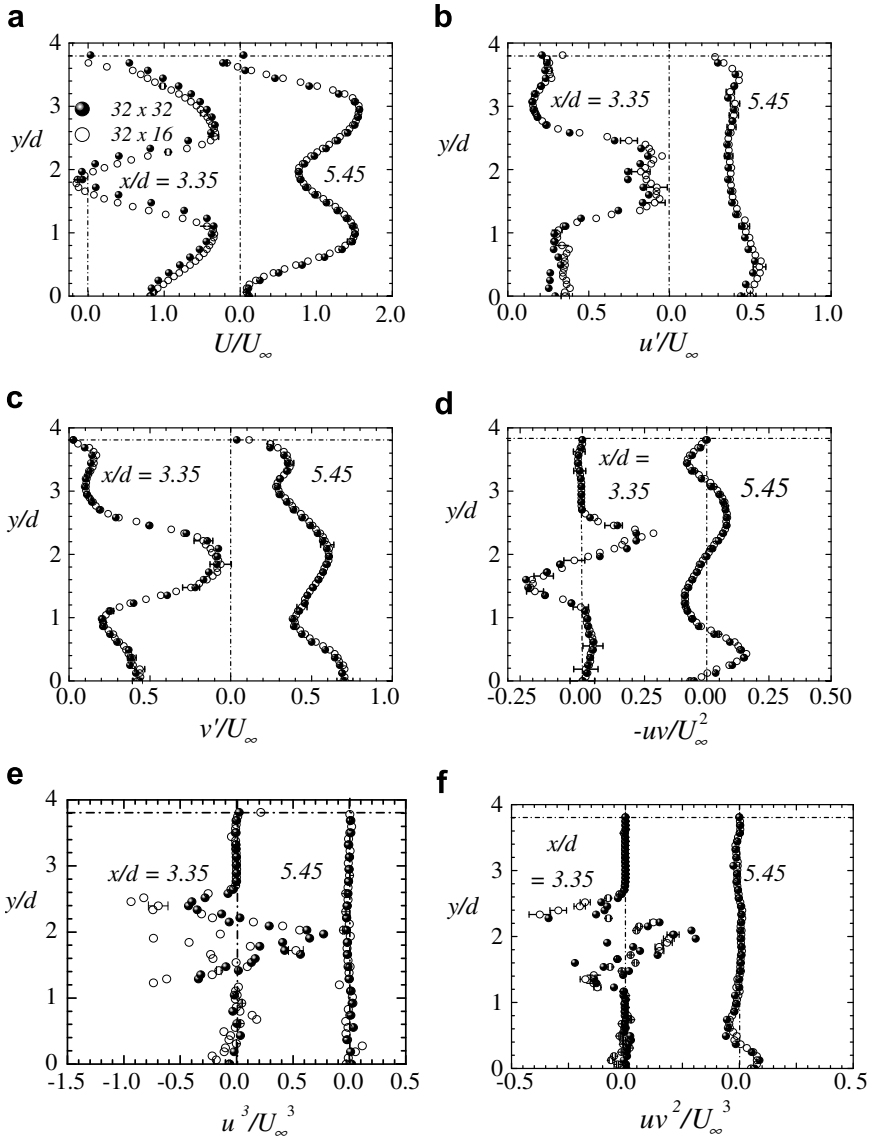

Fig. 2. Profiles of the mean velocity and turbulent quantities obtained using two interrogation areas: (a) U/U_∞, (b) u/U_∞, (c) v/U_∞, (d) $-\langle uv\rangle U_\infty^2$, (e) u^3/U_∞^3 and (f) uv^2/U_∞^3. The error bar in this and subsequent figures denote measurement uncertainty at 95% confidence level.

at $x/d = 3.35$ ($1.3 \leqslant y/d \leqslant 2.5$, approximately). It is noticed that the profiles of the dissipation term in Fig. 3b shows significant variation at the two x/d locations. This is because the rate of turbulence dissipation occurs at the smallest scales. It should be noted that the spatial resolution or spacing between data points is limited to 0.78 mm, which is much larger than the Kolmogorov length scale, estimated to be $\eta = 30$ μm. Although the present spatial resolution is above the scale expected to precisely measure the dissipation rate, profiles of dissipation rate will be presented to qualitatively show how it varies within the tube bundle. All the results presented subsequently are those obtained from the smaller (32×16 pixels) interrogation area size because it is believed that the dissipation rate obtained from this particular interrogation area is closer to the true values.

3. Numerical modeling

Problem definition: The geometry of the two-dimensional domain representing a typical region in a bundle with tube diameter d, transverse pitch, S_T, and longitudinal pitch, S_L, is shown in Fig. 4a. Fluid with an approach velocity, U_∞, enters the solution domain uniformly at the inlet region, a distance L_{us} from the center of the first tube. The outlet section is placed a distance L_{ds} from the center of the last tube. The values of L_{us} and L_{ds} are taken to be 10 d and 10 d, respectively. These values were chosen so that their location did not have a significant impact on the solutions obtained. The full number of tubes in the present experimental study is modeled and, due to symmetry, the computational domain is half of the experimental domain.

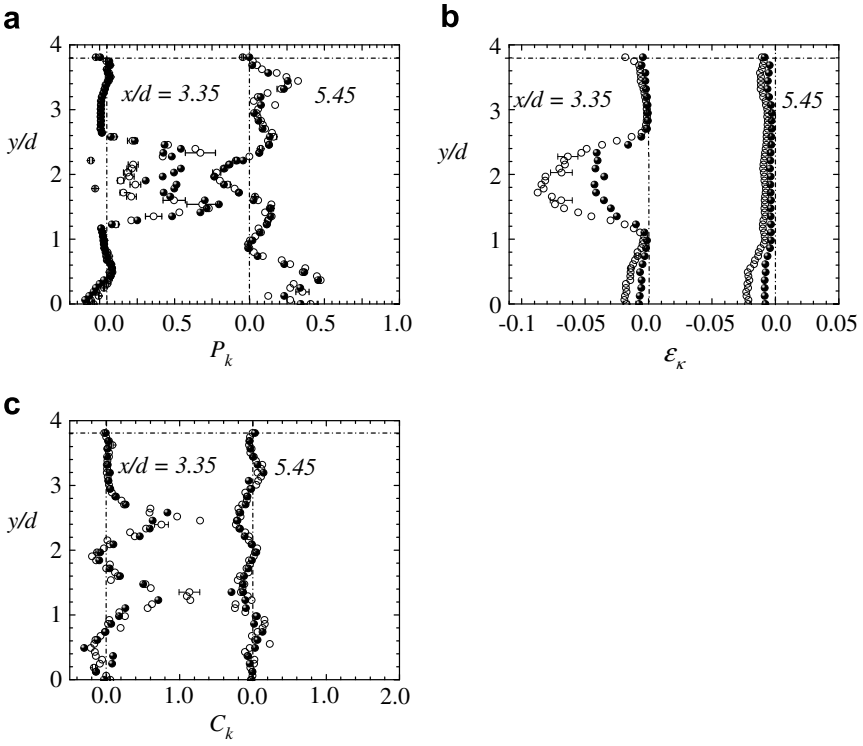

Fig. 3. Profiles of the turbulent kinetic energy budget: (a) P_k, (b) ε_k, and C_k. All terms are non-dimensionalized by U_∞^3/d. Symbols are as in Fig. 2.

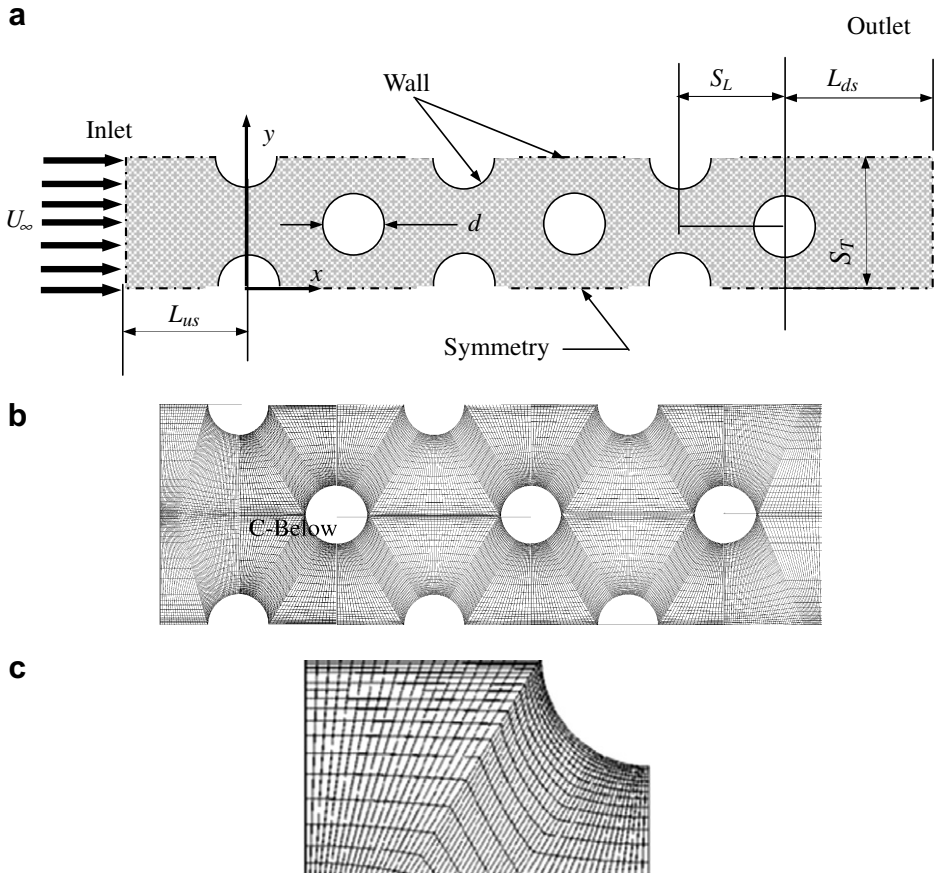

Fig. 4. (a) Solution domain nomenclature, (b) computational grid, and (c) sample grid detail (coarse mesh).

3.1. Computational mesh

Structured, non-orthogonal, non-uniform, boundary-fitted grids were generated for the solution domain shown in Fig. 4a. All the structured grids used were generated using TASCgrid, the grid generation component of CFX-TASCflow v2.12, and then imported into ANSYS CFX. The grid generation software uses transfinite interpolation to compute the mesh. The grids were created on a region-by-region basis, and then attached together as needed. Rectangular sections were generated for the upstream and downstream sections, and five different inter-tube region grids were created. Based on a coarse grid example, the assembly of the grid in the tube bundle region for the domain modeled is shown in Fig. 4b. Fig. 4c is a sample grid detail (coarse mesh) of the section indicated in Fig. 4b. Grid refinement near the tube surfaces and the wall was achieved by using a geometric grid expansion and contraction factor.

3.2. Governing equations

The flow is considered to be two-dimensional, incompressible, isothermal, steady, and turbulent. The fluid is Newtonian with constant density, ρ, and dynamic viscosity, μ. The Reynolds Averaged Navier–Stokes (RANS) equations for continuity and momentum conservation can be written as

$$\frac{\partial U_j}{\partial x_j} = 0 \tag{5}$$

$$\frac{\partial}{\partial x_j}(\rho U_j U_i) = -\frac{\partial P}{\partial x_i} + \frac{\partial}{\partial x_j}\left(\mu\frac{\partial U_i}{\partial x_j} - \rho\overline{u_i u_j}\right) \tag{6}$$

where $\overline{u_i u_j}$ is the Reynolds stress tensor. The mean flow pressure is P, and the mean velocity component in the x_i direction is U_i. The turbulence models used to compute the Reynolds stress tensor are discussed below.

3.3. Turbulence models

The four turbulence models used in this study are three two-equation models and one Reynolds stress model. The two-equation models are the k–ε developed by Launder and Spalding (1994), the k–ω by Wilcox (1988) and the shear stress transport (SST) k–ω based model developed by Menter (1994). The Reynolds stress model is the ε-based second moment closure model developed by Launder et al. (1975). These models will be referred to hereafter as k–ε, k–ω, SST, and LRR-IP, respectively. The two-equation models assumed eddy–viscosity relationship for the Reynolds stresses in Eq. (6), given by

$$-\rho\overline{u_i u_j} = \mu_t\left(\frac{\partial U_i}{\partial x_j} + \frac{\partial U_j}{\partial x_i}\right) - \frac{2}{3}\rho\delta_{ij}k \tag{7}$$

where μ_t is the eddy viscosity and δ_{ij} is the Kronecker delta. The pressure includes $\frac{2}{3}\rho\delta_{ij}k$ coming from the Reynolds stresses. The transport equations and auxiliary relations of the two-equation models are shown in Table 2. Table 3 shows the details of the Reynolds Stress model.

3.4. Boundary conditions

The boundary conditions for the solution domain shown in Fig. 4b are as follows. At the inlet, an average upstream value of the mean velocity equal to the approach velocity, $U_\infty = 0.34$ m/s obtained from measurement is specified along with $V = 0$. It is noted that the boundary layer thickness in the measured data is significant; however, a uniform approach is used for simplicity. In addition, at the inlet the relative turbulence intensity, based on the experimental data, is set equal to 4%. ANSYS CFX V10.0 computes the dissipation rate from turbulent viscosity ratio (μ_t/μ) using $\varepsilon = C_\mu\rho k^2/\mu_t$ and $\mu_t/\mu = 1000I$, where I is the turbulence intensity. On the constant y surface at $y = 0$, a symmetry boundary condition was applied. A stationary wall (no-slip) boundary condition was prescribed on the constant y surface at $y = S_T$ and at the arc-shaped boundaries representing the tube surfaces. In the k–ε and LRR-IP models, a scalable wall function approach is used for the near-wall treatment. The fundamental principle of the scalable wall function approach used in CFX (Grotjans and Menter, 1998), is to limit the y^+ value used in the logarithmic formulation by a lower value of $\tilde{y}^+ = \max(y^+, 11.06)$, where 11.06 is the intersection of the logarithmic and linear near wall profiles. The computed $\tilde{y}^+$ value is not allowed to fall below this limit, therefore, all mesh points are outside of the viscous sublayer and all fine mesh inconsistencies are avoided. The flux boundary conditions applied at the wall for the scalable wall-function approach used in CFX are as follows:

$$\mu_t\frac{\partial U}{\partial n} = -\rho u_\tau \max(|u_\tau|, u^*) \tag{8}$$

$$\frac{\partial k}{\partial n} = 0 \tag{9}$$

$$\frac{\mu_\tau}{\sigma_\varepsilon}\frac{\partial \varepsilon}{\partial n} = -\frac{1}{\sigma_\varepsilon}\frac{(u^*)^5\rho^2}{\tilde{y}^+\mu} \times \left[\frac{2+e}{2+2e}\right] + F_{\text{cal}}\frac{e}{2}\frac{\sigma_\varepsilon\sqrt{C_\mu}}{\kappa^2}(C_{\varepsilon 2} - C_{\varepsilon 1}) \tag{10}$$

$$\text{with} \quad e = \frac{\Delta y^+}{\tilde{y}^+} \tag{11}$$

$$\text{and} \quad u^* = C_\mu^{1/4}k^{1/2} \tag{12}$$

Here Δy^+ is the actual y^+ value from the wall to the first interior node, F_{cal} is a calibration function based on the coarseness of the mesh, and u^* is an alternative velocity scale used to prevent the flux from going to zero at separation points (as was a problem with standard wall-functions). A near-wall treatment that switches automatically, based on grid refinement, from wall function to low-Reynolds number formulation is employed for k–ω and SST models. These sets of wall treatments were the only avail-

Table 2
Transport equations and auxiliary relations of the two-equation models

Model equation	Closure coefficients and auxiliary relations
k–ε model	Production term, P_k, is for all models:
$\frac{\partial}{\partial x_j}(\rho U_j k) = \frac{\partial}{\partial x_j}\left(\left(\mu + \frac{\mu_t}{\sigma_k}\right)\frac{\partial k}{\partial x_j}\right) + P_k - \rho\varepsilon$ $\frac{\partial}{\partial x_j}(\rho U_j \varepsilon) = \frac{\partial}{\partial x_j}\left(\left(\mu + \frac{\mu_t}{\sigma_\varepsilon}\right)\frac{\partial \varepsilon}{\partial x_j}\right) + \frac{\varepsilon}{k}(C_{\varepsilon 1} - \rho C_{\varepsilon 2}\varepsilon)$	$P_k = \mu_t\left(\frac{\partial U_i}{\partial x_j} + \frac{\partial U_j}{\partial x_i}\right)\frac{\partial U_i}{\partial x_j}$
k–ω model	Turbulent viscosity For k–ε: $\mu_t = \rho C_\mu k^2/\varepsilon$ For k–ω: $\mu_t = \rho(k/\omega)$ For SST: $\mu_t = \frac{\rho a_1 k}{\max(a_1\omega, SF_2)}$
$\frac{\partial}{\partial x_j}(\rho U_j k) = \frac{\partial}{\partial x_j}\left(\left(\mu + \frac{\mu_t}{\sigma_k}\right)\frac{\partial k}{\partial x_j}\right) + P_k - \rho\beta^* k\omega$ $\frac{\partial}{\partial x_j}(\rho U_j \omega) = \frac{\partial}{\partial x_j}\left(\left(\mu + \frac{\mu_t}{\sigma_\omega}\right)\frac{\partial \omega}{\partial x_j}\right) + \alpha\frac{\omega}{k}P_k - \rho\beta\omega^2$	
SST model	For SST: The blending function, F_1, is given by:
$\frac{\partial(\rho U_j k)}{\partial x_j} = \frac{\partial}{\partial x_j}\left(\left(\mu + \frac{\mu_t}{\sigma_{k_2}}\right)\frac{\partial k}{\partial x_j}\right) + P_k - \beta^*\rho k\omega$ $\frac{\partial(\rho U_j \omega)}{\partial x_j} = \frac{\partial}{\partial x_j}\left(\left(\mu + \frac{\mu_t}{\sigma_{\omega_2}}\right)\frac{\partial \omega}{\partial x_j}\right) + (1-F_1)2\rho\frac{1}{\sigma_{\omega 2}\omega}\frac{\partial k}{\partial x_j}\frac{\partial \omega}{\partial x_j} + \alpha_2\frac{\omega}{k}P_k - \rho\beta_2\omega^2$	$F_1 = \tanh(\arg_1^4)$ with $\arg_1 = \min\left(\max\left(\frac{\sqrt{k}}{\beta^*\omega y}, \frac{500v}{y^2\omega}\right), \frac{4\rho k}{CD_{k\omega}\sigma_{\omega 2} y^2}\right)$ $CD_{k\omega} = \max\left(2\rho\frac{1}{\sigma_{\omega 2}\omega}\frac{\partial k}{\partial x_j}\frac{\partial \omega}{\partial x_j}, 1.0\times 10^{-10}\right)$ and $F_2 = \tanh(\arg_2^2)$ with $\arg_2 = \max\left(\frac{2\sqrt{k}}{\beta^*\omega y}, \frac{500v}{y^2\omega}\right)$ $S = \sqrt{\left(\frac{\partial U_i}{\partial x_j} + \frac{\partial U_j}{\partial x_i}\right)\frac{\partial U_i}{\partial x_j}}$

Constants:
For k–ε: $C_{\varepsilon 1} = 1.44$, $C_{\varepsilon 2} = 1.92$, $\sigma_k = 1.0$, $\sigma_\varepsilon = 1.3$, $C_\mu = 0.09$
For k–ω: $\beta^* = 0.09$, $\beta = 0.075$, $\alpha = 5/9$, $\sigma_\omega = 2$, $\sigma_k = 2$
For SST: $\alpha_2 = 0.44$, $\sigma_{\omega 2} = 10.856$, $\sigma_{k2} = 1$, $\beta_2 = 0.0828$, $\beta^* = 0.09$, $a_1 = 0.31$

Table 3
Transport equations and auxiliary relations of the Reynolds stress model

Reynolds stress model (LRR-IP)	
$\frac{\partial}{\partial x_k}(U_k\overline{\rho u_i u_i}u_j) = \frac{\partial}{\partial x_k}\left\{\left(\mu + \frac{2}{3}C_s\rho\frac{k^2}{\varepsilon}\right)\frac{\partial}{\partial x_k}(\overline{\rho u_i}u_j)\right\} - \overline{\rho u_k u_i}\frac{\partial U_i}{\partial x_j} - \overline{\rho u_k u_j}\frac{\partial U_i}{\partial x_k} + \phi_{ij} - \frac{2}{3}\delta_{ij}\rho\varepsilon$ $\frac{\partial}{\partial x_j}(\rho U_j\varepsilon) = \frac{\partial}{\partial x_j}\left(\left(\mu + \frac{\mu_t}{\sigma_\varepsilon}\right)\frac{\partial \varepsilon}{\partial x_j}\right) + \frac{\varepsilon}{k}\left(C_{\varepsilon 1}\left(-\rho\overline{u_i u_j}\frac{\partial U_i}{\partial x_j}\right) - C_{\varepsilon 2}\rho\varepsilon\right)$	$a_{ij} = \frac{\overline{u_i u_j}}{k} - \frac{2}{3}\delta_{ij}$ $S_{ij} = \frac{1}{2}\left(\frac{\partial U_i}{\partial x_j} + \frac{\partial U_j}{\partial x_i}\right)$ $W_{ij} = \frac{1}{2}\left(\frac{\partial U_i}{\partial x_j} - \frac{\partial U_j}{\partial x_i}\right)$
The pressure–strain term, ϕ_{ij}, is modeled using: $\phi_{ij} = -\rho\varepsilon C_{s1}a_{ij} + C_{r2}\rho k S_{ij} + C_{r4}\rho k\left(a_{ik}S_{jk} + a_{jk}S_{ik} - \frac{2}{3}a_{kl}S_{kl}\delta_{ij}\right) + C_{r5}\rho k(a_{ik}W_{jk} + a_{jk}W_{ik})$	Constants: $C_s = 0.22$, $C_{s1} = 1.8$, $C_{r2} = 0.8$, $C_{r4} = 0.6$, $C_{r5} = 0.6$, $C_{\varepsilon 1} = 1.45$, $C_{\varepsilon 2} = 1.90$, $\sigma_\varepsilon = 1.10$

able choices in the version of ANSYS CFX used. At the outlet, an outflow condition was prescribed with an average pressure at the entire outlet area set to a reference value of zero.

3.5. Numerical solution

The numerical solution of the governing equations was obtained using a commercial CFD code: ANSYS CFX V10.0. In this 3D-code, discretization is done based on a finite volume approach (Patankar, 1980), but the geometrical representation and integration points are based on a finite element approach. Mass conservation discretization was applied on a non-staggered grid with pressure–velocity coupling based on the work of Rhie and Chow (1983). The advection term discretization uses a numerical advection correction which may be viewed as an anti-diffusive flux added to the upwind scheme. The advection scheme implemented in the version of CFX used can be cast in the form $\phi_{ip} = \phi_{up} + \beta\nabla\phi \cdot \Delta\vec{s}$, where ϕ_{up} is the value at the upwind node, $\nabla\phi$ is the gradient of ϕ, and $\vec{s}$ is the vector from the upwind node to the *ip*. The second order accurate high resolution advection scheme, based on the work of Barth and Jesperson (1989), was employed in the present study. For this particular scheme, $\nabla\phi$ is the nodal gradient of the upwind node and $\beta = 1$. The discretized mass, momentum and turbulence model equations were solved iteratively using an additive correction multi-grid method to accelerate convergence. Double precision was used in the computations and the solution was considered converged when the normalized RMS residual of each of the discretized equations was less than 1.0×10^{-5}.

3.6. Mesh-independence tests

Mesh-independence tests were performed to investigate the influence of grid refinement on the solution and representative results are presented here for six of the computational grids used. Table 4 provides some details of the grids, including the total number of nodes, the numbers of nodes in the x- and y-directions, and the y-direction geometric expansion factor. The grid expansion factor, r_y, is the relative increase in grid spacing along the y-direction in a given grid segment, and was used to investigate the effect of refinement of the grid near boundaries in addition to the choice of Ny. In this application, the grid sub-regions were created before assembly with local y (transverse coordinate) defined in such a way that the grid expands away from all wall boundaries. A larger value of r_y indicates a greater rate of increase of grid spacing away from a boundary. For a fixed number of nodes across a region, a larger r_y produces nodes more closely spaced near a boundary, and a smaller first y-direction spacing near a wall. The set of grids shown in Table 4 shows a variation of Nx, Ny, and r_y, to assess separately the effect of changes in their values. Because of the choice of assembling the grid from structured-grid sub-regions around the tubes, certain choices of Nx, Ny, and r_y produced grids with skew angles and aspect ratios that led to convergence difficulties. Therefore, the set of six grids shown in Table 4 is the result of significant testing to obtain working grids that could be used to carefully examine grid independence of the solutions. Also shown in Table 4 are the maximum values in the domain of the standard y^+ and solver y-plus (denoted as y^+_{solver}) values obtained in post-processing for each of the models for each of the grids. The solver y-plus is an internally calculated y^+ value used in the CFX solver. It should be noted that Grid A is very coarse and has large $y^+_{\max}$ values that are in the logarithmic region for all four turbulence models. For the ε-based models (k–ε and LRR-IP), $y^+_{\max}$ is in the viscous sublayer ($y^+ < 5$) for Grids C, D, E and F. For the ω-based models (k–ω and SST), $y^+_{\max}$ is also in the viscous sublayer for Grid D and although the $y^+_{\max}$ values for Grids B, C, E and F are outside the viscous sublayer, they are well below $y^+ = 11$. Moreover, $y^+_{\text{solver,max}}$ values for the ε-based models are clipped to 11.06 as is consistent with the scalable wall function approach.

Samples of the results in the developing region ($x/d = 1.25$) and the spatially periodic region ($x/d = 5.45$) from computations using grids A, B, C, and D are shown in Figs. 5–7. The profiles of U in Fig. 5a to d show that the k–ε and LRR-IP models are not very sensitive to grid resolution changes beyond a certain resolution; in this case, for Grid B or finer. This trend is similar for the results for V and k shown in Figs. 6a–d and 7a–d, respectively. On the other hand, Fig. 5e–h show that the k–ω and SST models are quite sensitive to grid resolution changes. Not only is there a large change in results from Grid A to Grid B (as seen for the k–ε and LRR-IP models), there continue to be changes in the results for Grids C and D at certain locations. The results in Fig. 5e–h show that the sample U profiles are reasonably grid-independent near the symmetry plane and near the wall for Grids B, C, and D. In the

Table 4
Details of grids used in mesh-independence tests and their maximum y^+ values

Grid	Nodes	Nx	Ny	r_y	k–ε		*LRR-IP*		k–ω		*SST*	
					$y^+_{\max}$	$y^+_{\text{solver,max}}$	$y^+_{\max}$	$y^+_{\text{solver,max}}$	$y^+_{\max}$	$y^+_{\text{solver,max}}$	$y^+_{\max}$	$y^+_{\text{solver,max}}$
A	32364	522	62	1.2	48.83	14.04	42.16	12.87	42.71	58.18	39.45	45.87
B	72144	1002	172	1.05	7.35	11.06	6.79	11.06	9.05	8.80	9.14	8.90
C	232704	1152	202	1.05	4.90	11.06	4.48	11.06	6.59	6.48	6.59	6.43
D	474888	1684	282	1.05	1.75	11.06	1.59	11.06	2.62	2.61	2.58	2.57
E	119564	842	142	1.2	3.72	11.06	3.45	11.06	5.25	5.19	5.18	5.13
F	202404	1002	202	1.05	4.89	11.06	4.48	11.06	6.59	6.47	6.53	6.43

Because ANSYS CFX is a 3D code, all grids contains three grid points in the spanwise direction. Symmetry was used in the spanwise direction, so this had no impact on the results. The x-direction grid expansion factor for all grids is $r_x = 0.98$.

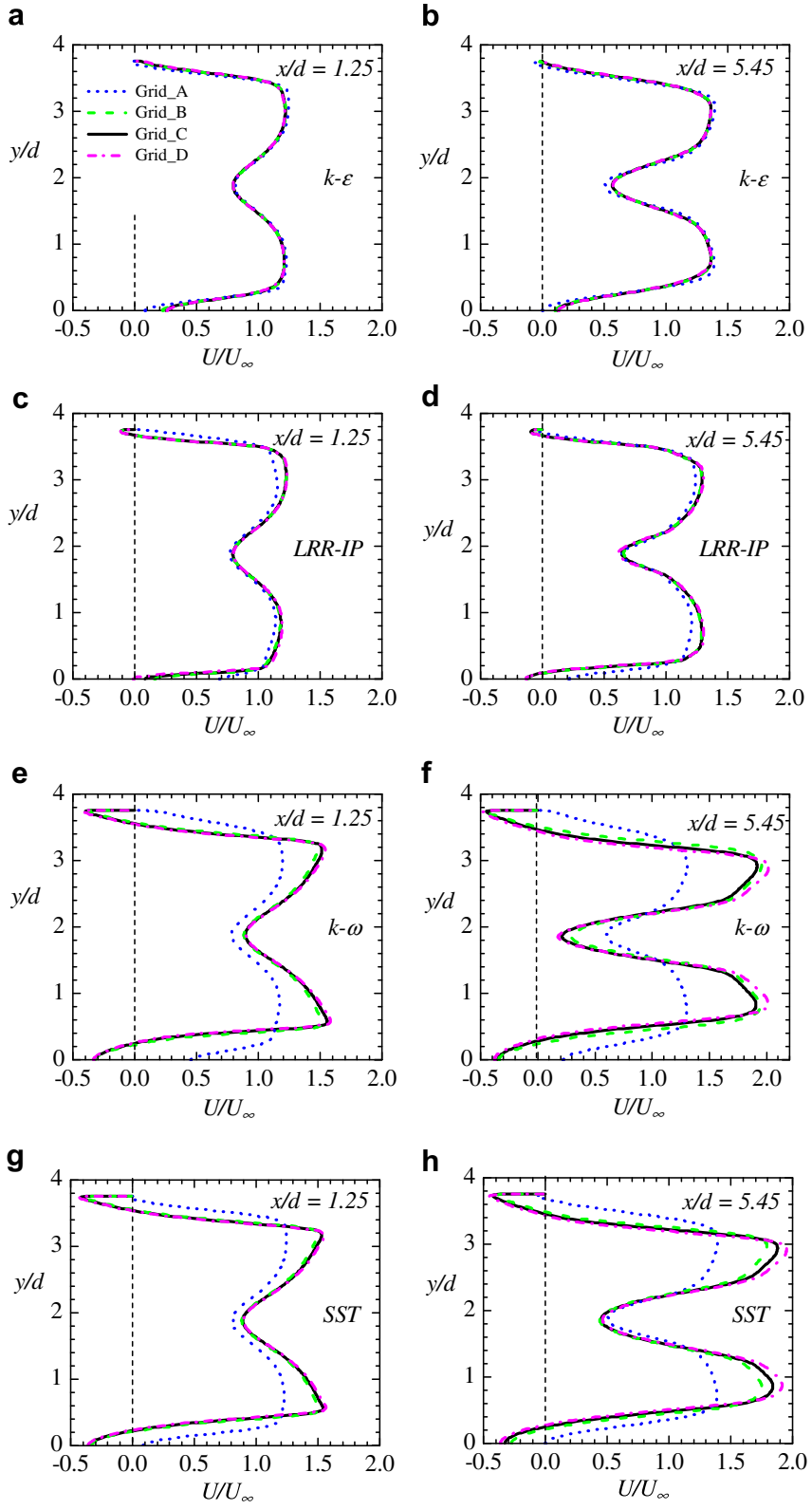

Fig. 5. Sample profiles of grid-independence test of streamwise mean velocity at $x/d = 1.25$ and 5.45: (a and b) k–ε; (c and d) *LRR-IP*; (e and f) k–ω; and (g and h) *SST*.

region around the two velocity peaks ($0.5 < y/d < 3.0$), however, there is a much greater sensitivity to changes in the grid resolution. These results indicate that grid refinement is needed not only near the wall, but also in the region between tubes. The profiles of V and k for the k–ω and SST models, shown in Figs. 6e–h and 7e–h, respectively, are

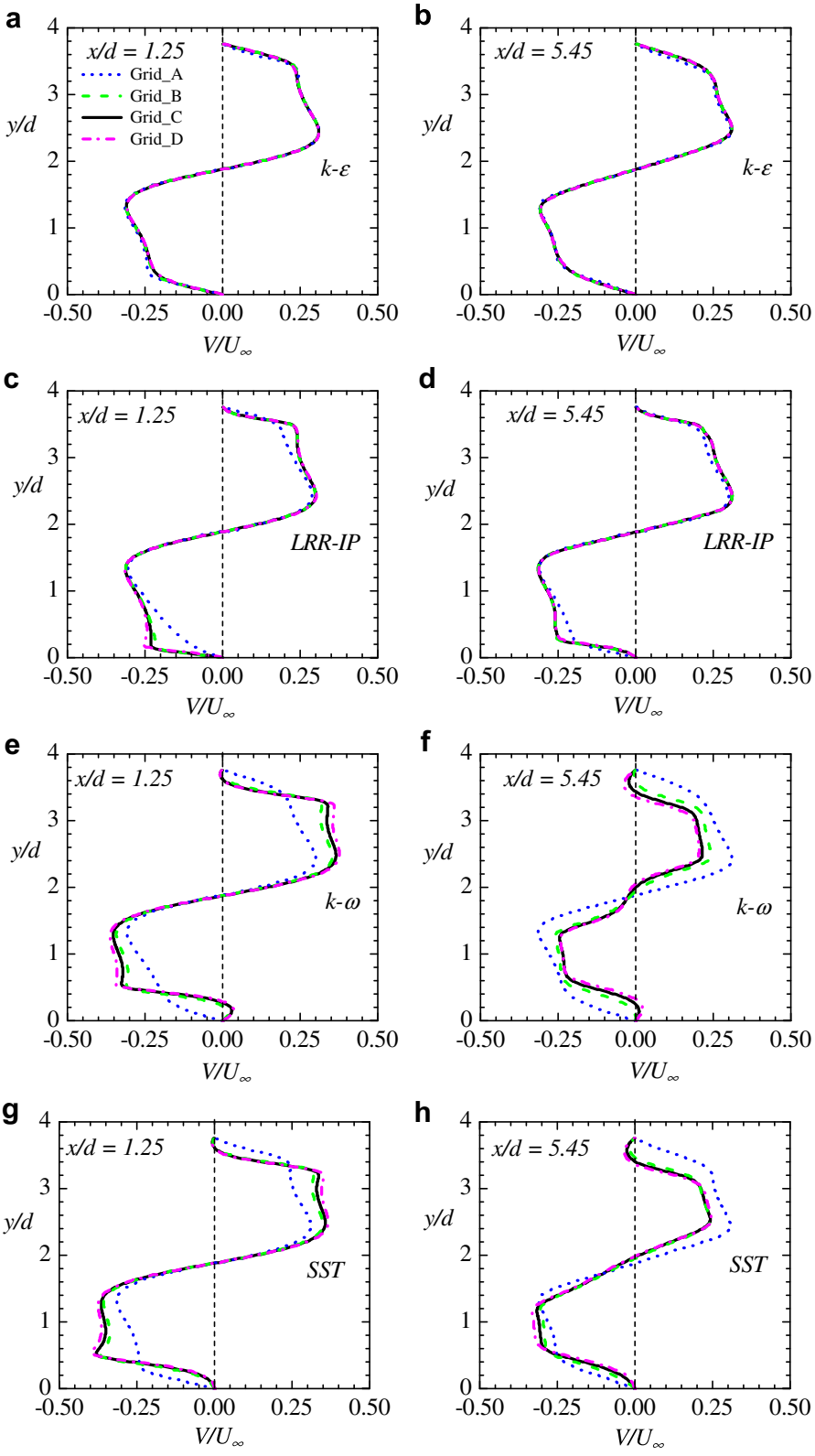

Fig. 6. Sample profiles of grid-independence test of transverse mean velocity at $x/d = 1.25$ and 5.45: (a and b) k–ε; (c and d) *LRR-IP*; (e and f) k–ω; and (g and h) *SST*.

consistent with these observations. It was also observed that there tends to be greater changes with grid resolution in the k–ω and SST model results at $x/d = 5.45$ than at $x/d = 1.25$.

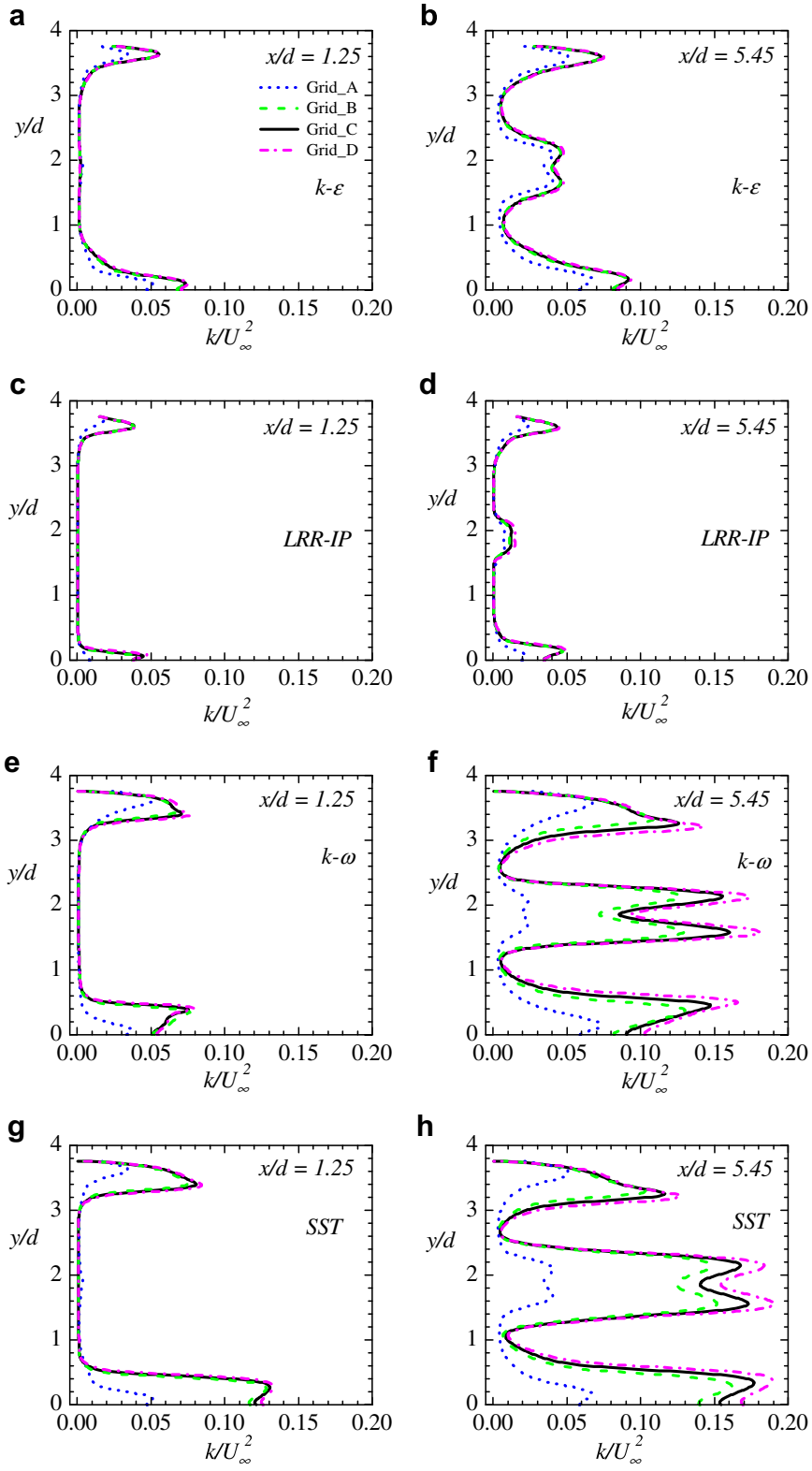

Fig. 7. Sample profiles of grid-independence test of turbulent kinetic energy at $x/d = 1.25$ and 5.45: (a and b) k–ε; (c and d) *LRR-IP*; (e and f) k–ω; and (g and h) *SST*.

Table 5 is a summary of representative values of the percentage deviations for results obtained using Grids A, B and D compared with the results from Grid C. When compiling the data for Table 5, it was recognized that there were two cases where percentage differences may be misleading. The first case occurred when field values were near

Table 5
Details of maximum deviations for present results using various meshes

Model	Grid	Maximum percent difference with respect to Grid C			y/d locations of maximum difference		
		U	V	k	U	V	k
$x/d = 1.25$							
k–ε	A	−1.86	−4.43	38.22	3.00	0.50	3.64
	B	−0.25	−0.90	1.45	2.96	0.50	3.64
	D	0.22	0.52	−2.33	2.93	0.50	0.09
LRR-IP	A	6.32	24.19	82.38	2.99	0.50	0.07
	B	0.72	2.46	5.70	0.50	0.50	0.07
	D	−1.52	−3.92	−4.49	0.50	0.50	0.07
k–ω	A	26.39	36.24	93.72	0.55	0.52	0.39
	B	2.94	5.78	7.31	0.61	3.00	3.42
	D	2.47	−6.19	−6.09	0.50	0.59	3.42
SST	A	21.17	35.69	89.70	0.55	0.52	3.40
	B	2.23	4.48	7.19	0.58	0.61	3.40
	D	−1.77	−4.57	−4.35	0.59	0.59	3.40
$x/d = 5.45$							
k–ε	A	−6.89	−4.97	30.04	2.30	1.47	3.59
	B	−0.86	−0.71	1.54	0.50	0.50	3.59
	D	0.94	0.93	−3.36	0.51	1.41	1.66
LRR-IP	A	8.25	15.61	67.50	0.50	0.50	0.15
	B	0.50	−0.41	0.88	1.54	1.60	3.59
	D	−1.12	1.61	−2.10	0.59	1.60	3.59
k–ω	A	−36.64	−180.53	89.39	1.60	1.60	1.57
	B	−26.71	−32.96	29.78	0.50	0.50	3.25
	D	22.80	24.38	−12.83	0.50	0.50	1.57
SST	A	26.36	−63.15	88.17	2.89	2.30	3.25
	B	−14.72	−6.84	17.85	0.50	0.50	3.25
	D	14.44	7.73	−10.45	0.50	0.50	1.55

zero. The second case occurred in regions where the results of different grids have very similar predictions of a steep field gradient, but are shifted slightly in the y-direction relative to each other (for example, in the region $0.2 < y/d < 0.5$ in Fig. 5f). The slight shift in profiles can cause very large local percentage differences, even though the overall predictions are very similar. These two drawbacks were avoided by restricting the regions over which percentage error are reported in Table 5 as follows. For U and V, the regions considered for Table 5 data were $0.5 \leqslant y/d \leqslant 1.6$ and $2.3 \leqslant y/d \leqslant 3.0$, and the maximum local percentage differences in these ranges are reported in Table 5. For k, the changes at the locations of the local maxima in the fields were considered, and the maximum local percentage difference is reported for each grid. The data in Table 5, therefore, are expected to represent fairly the cases where changes are relatively small between sets of results, and others where changes are significant. For all percentage differences in Table 5, the corresponding y/d locations where these maximum deviations occurred are also reported. In the following discussion of Table 5 data, the references to values of percentage difference will imply the magnitude of the percentage difference. The data in Table 5 indicate that the representative percentage differences obtained from k–ε and LRR-IP models for Grids B and D at both x/d locations are less than 4% for U and V and 6% for k. These comparisons indicate reasonable mesh independence of the k–ε and LRR-IP models for Grids B, C, and D.

The results for the k–ω and SST models, on the other hand, show somewhat higher differences for Grids B and D, especially at $x/d = 5.45$, as mentioned earlier. For U, the differences at $x/d = 1.25$ are less than 3%, but at $x/d = 5.45$, the differences are in the range 14–27%. It should be noted, however, that these larger differences at $x/d = 5.45$ occurred at the lower limit of the range of consideration ($y/d = 0.5$) where the overall agreement is reasonable, but the profiles are shifted in y with respect to each other. For V, the differences are mostly less than about 6% at $x/d = 1.25$. At $x/d = 5.45$, the differences for Grids B and D for the SST model are roughly 7% and 8%, respectively, while those for the k–ω model are approximately 33% and 24%. These larger differences arise under the same conditions as discussed above for U. For the k–ω and SST models, the maximum differences in k at $x/d = 1.25$ are less than roughly 7%. At $x/d = 5.45$, however, the differences are in the range 11–30%. Given that the relatively higher deviations from the k–ω and SST models are still reasonable for U and V, and that the larger differences in k occur only at a few localized areas in the plots, it is believed that Grid C is fine enough to produce reasonable results.

Finally, comparisons between the results using Grids C, E, and F in the profiles of U and k at selected x/d locations were made on the results for the k–ε and k–ω models, in order to examine the effects of changes in the y-direction grid expansion and the x-direction grid resolution. There were no significant differences in the results for the three grids. It was therefore observed that reasonable results

can be obtained when using fewer nodes in the y-direction provided a larger grid expansion factor is used. Based on the above results and similar checks in other cases, Grid C was selected for the present investigation. All the remaining results presented here are based on Grid C.

4. Results and discussion

The prediction for the entire domain in Fig. 4b was performed. However, for the purpose of comparison with experimental data, only profiles obtained at the selected x/d locations shown in Fig. 1b are presented. In the presentation of results, the approach velocity, U_∞, is used to normalize both the mean velocities and the turbulence quantities.

4.1. Mean velocity

4.1.1. Wake and impact regions

Fig. 8 compares predicted and measured values of the streamwise mean velocity in regions along the centerline ($y = 0$) just behind tubes 1 and 3 (wake_row1 and wake_row3) and just in front of tubes 3 and 5 (impact_row3 and impact_row5). The distribution of the streamwise component of the mean velocity along the wake center line provides information about the recovery of the streamwise mean velocity as well as the length of the recirculation zone. Balabani (1996) defined the recirculation length, l_r, as the distance between the tube rear surface and the point of zero streamwise mean velocity. This corresponds to the distances between points $x/d = 0.5$ and 1.5 and between $x/d = 4.7$ and 5.4 in curves wake_row1 and wake_row3, respectively, for the measured values in Fig. 8a and b. The results indicate that the four turbulence models predicted the correct trends of the mean velocity profiles in the recirculation zones, but failed to predict the correct sizes of the recirculation zones. The k–ε model predicts a too small recirculation length (about 25% of the measured values in the two wake regions), which is consistent with the experience of Meyer (1994). The discrepancy might be attributed to the insensitivity of the standard k–ε model to streamline curvature. At wake_row1, the LRR-IP

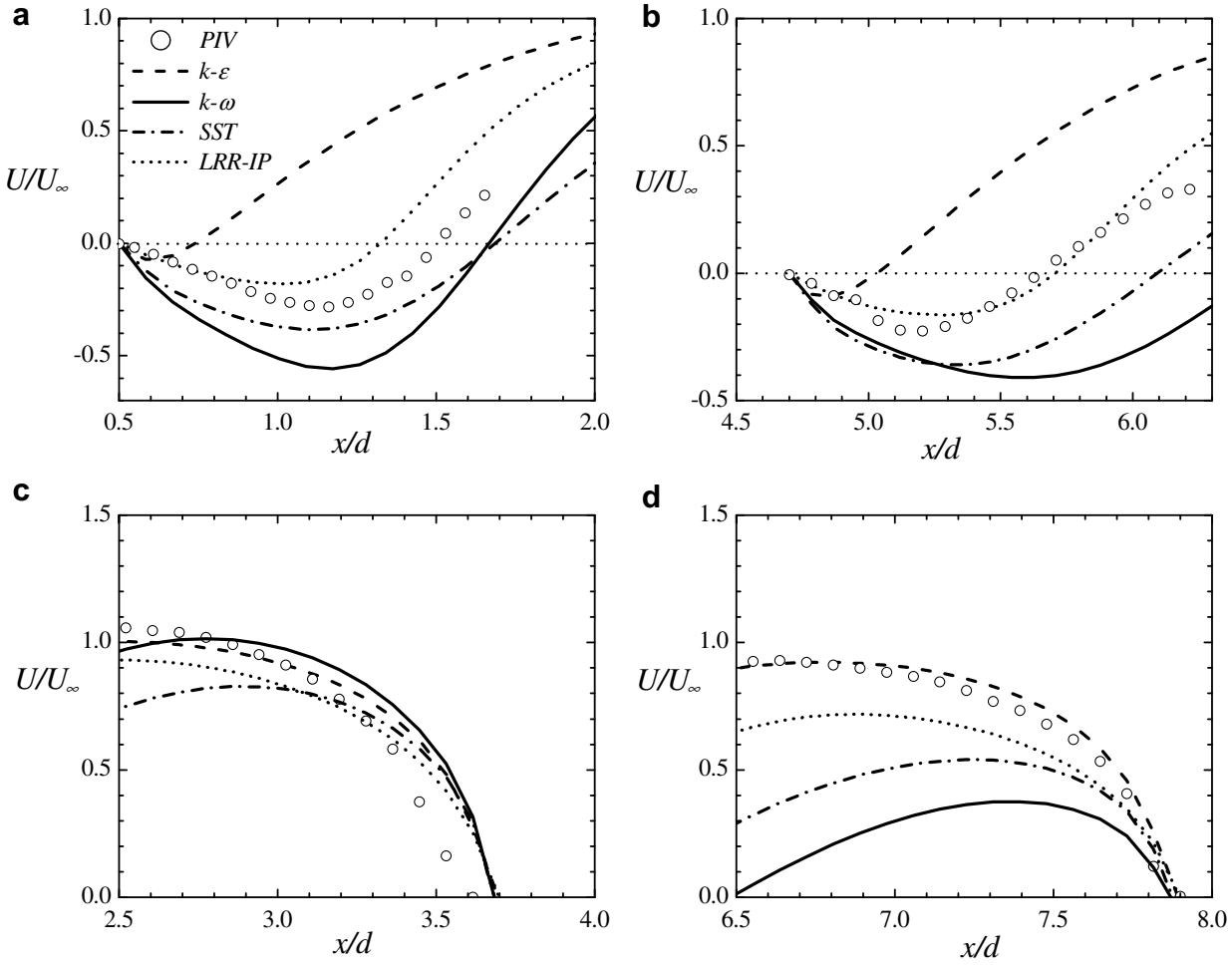

Fig. 8. Comparison between profiles obtained from the present prediction of the mean velocity with measured values at: (a) wake_row1 and (b) wake_row3, (c) impact-row3 and (d) impact-row5.

model, which is also an ε-based model, underpredicted l_r by about 20%. The two ω-based models (SST and k–ω), on the other hand, overpredicted l_r by about 20%. At wake_row3, the LRR-IP, SST and k–ω all overpredicted l_r significantly. Fig. 8c reveals that all the turbulence models predicted the mean velocity profiles in impact_row3

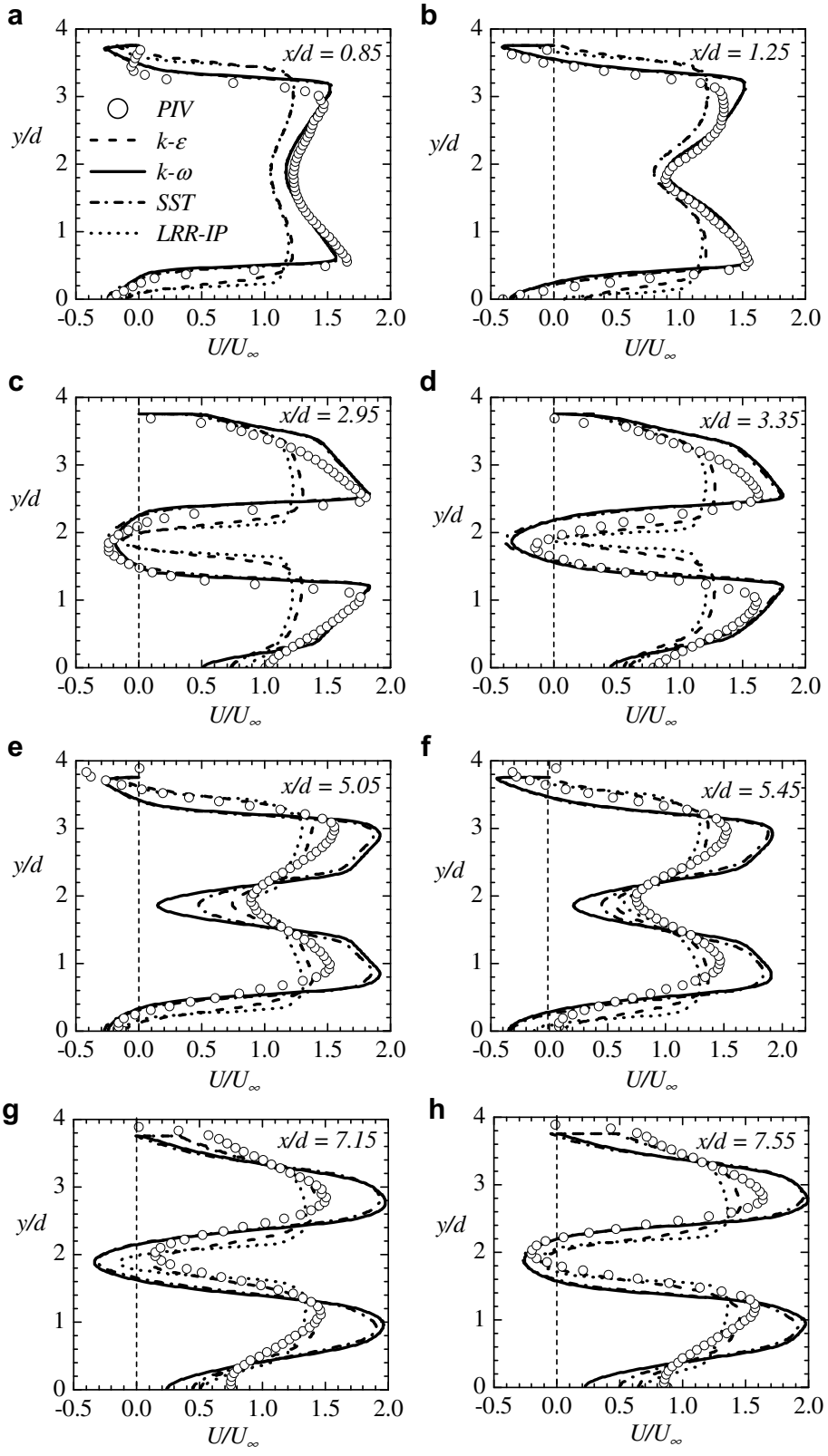

Fig. 9. Comparison between profiles of predicted streamwise mean velocity with measured values at selected axial locations.

fairly well. In impact_row5 (Fig. 8d), results from the k–ε model are in excellent agreement with measured mean velocity profiles. The LRR-IP model underpredicted by about 20% but results obtained from the SST and k–ω models are significantly lower than measured data. It is clear from Fig. 8 that none of the models used in this study provides consistently good results in both the wake and impact regions.

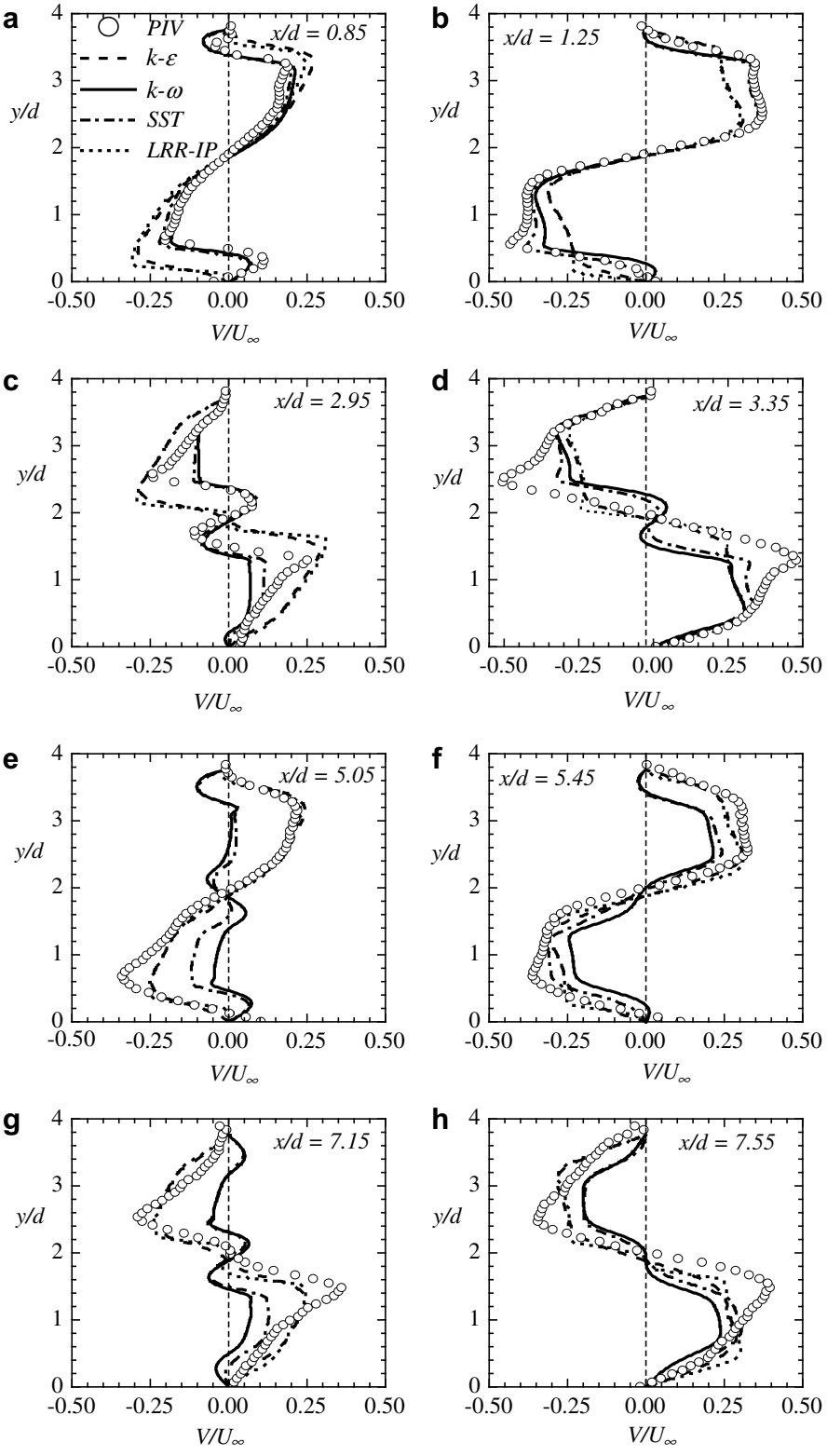

Fig. 10. Comparison between profiles of predicted transverse mean velocity with measured values at some axial locations.

4.1.2. Constant x/d locations

The distribution of the dimensionless streamwise and transverse mean velocities at selected x/d locations are shown in Figs. 9 and 10, respectively. Fig. 9 reveals that all the turbulence models produce the correct trends of the streamwise mean velocity profiles at all x/d locations. However, results

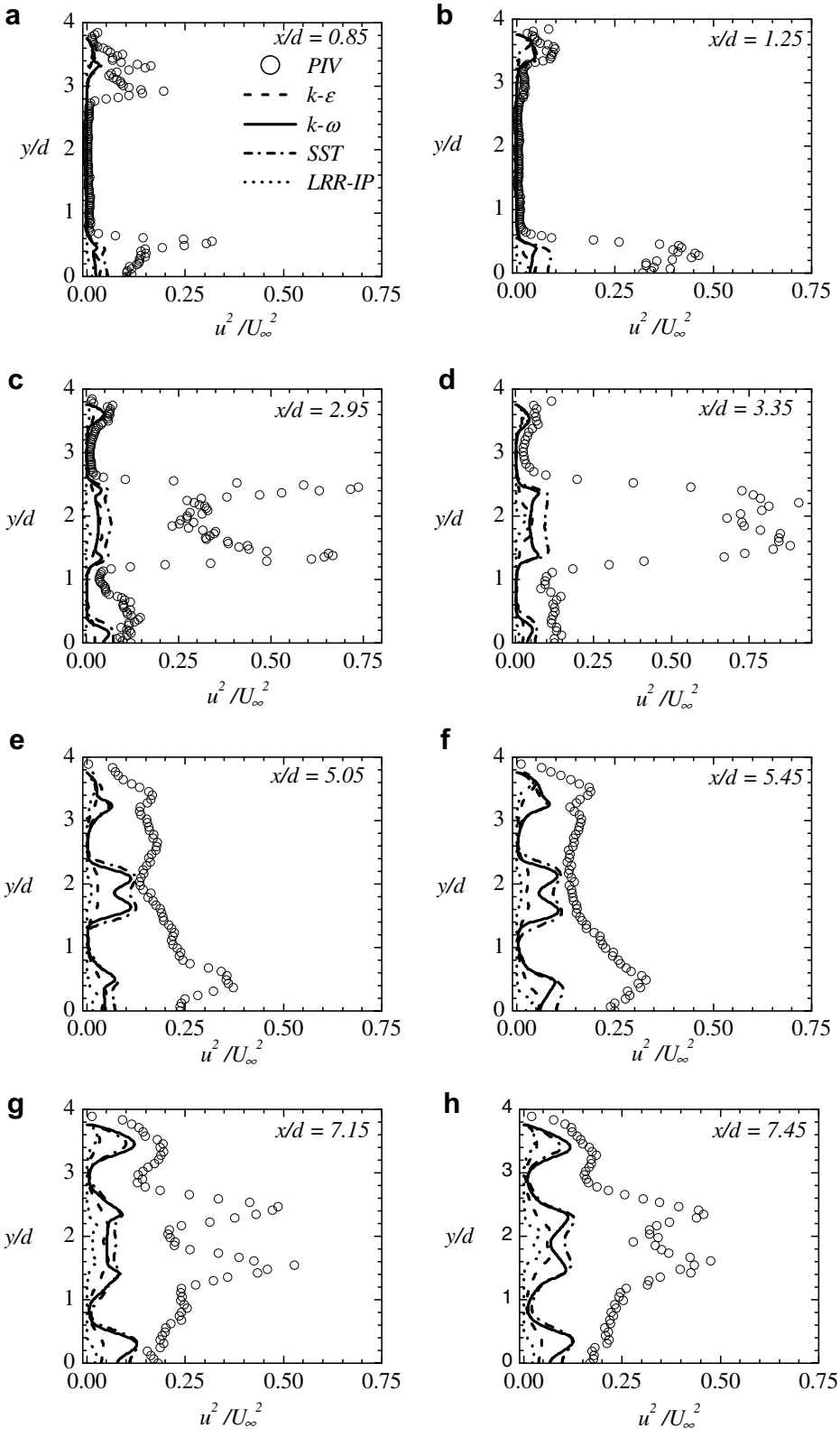

Fig. 11. Comparison between profiles of streamwise normal stresses predicted with measured values at selected x/d locations.

from the ω-based models appear to be in better agreement with the experimental data in the flow developing region (i.e., $x/d = 0.85$–3.35) while the ε-based models perform better in the spatially periodic region (i.e., $x/d \geqslant 5.05$). This behavior of the ω-based models might be due to their late recovery of the flow separation, which was observed in Fig. 8.

The measured mean velocity profiles shown in Fig. 9a and b revealed lower peak values close to the channel wall

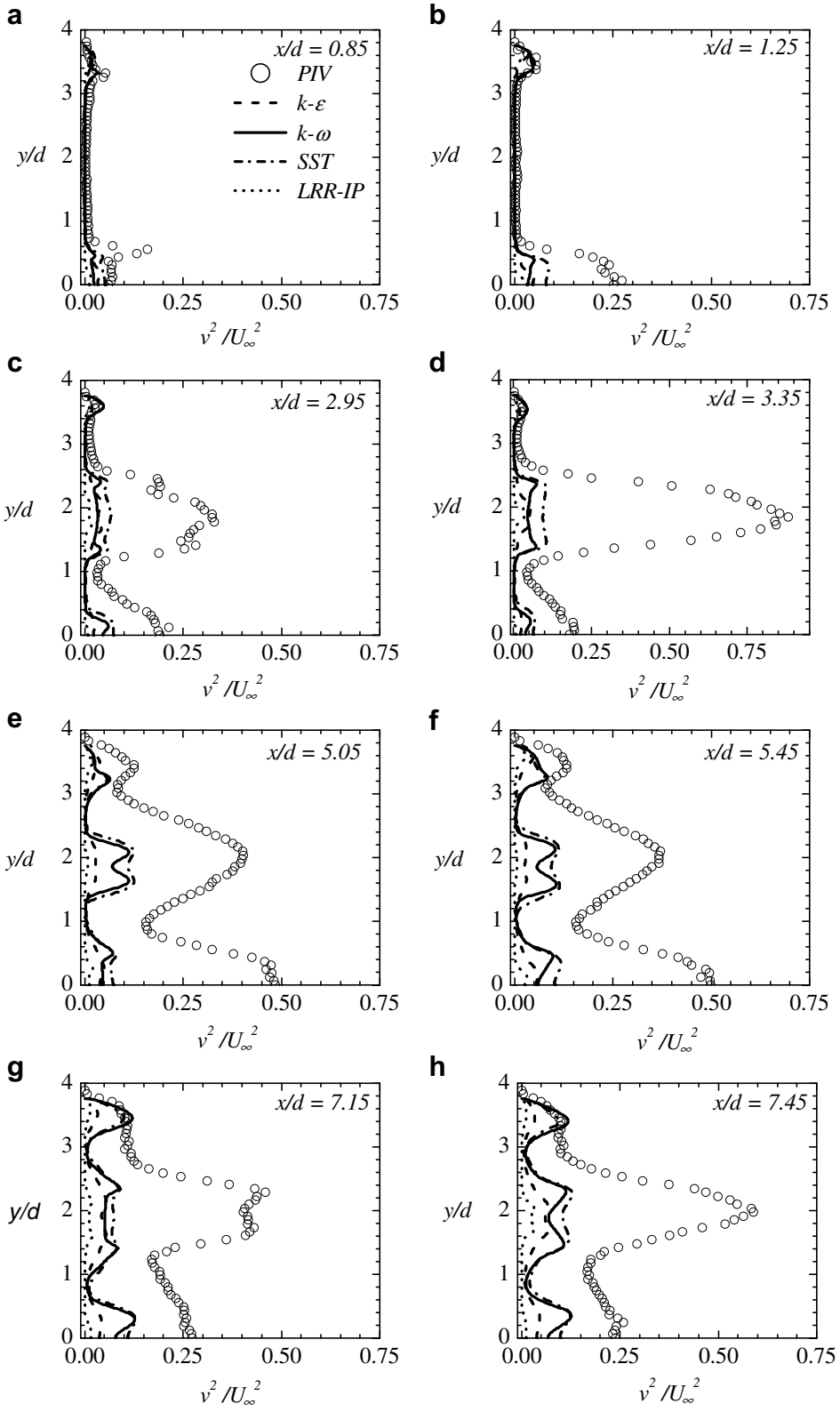

Fig. 12. Comparison between the predicted transverse normal stresses with measured values at selected x/d locations.

than in the central portion of the flow. At these locations, the numerical results, however, produced similar peak values perhaps due to the uniform profiles employed at the inlet section of the computational domain. Fig. 10 shows that the trends of the predictions of the transverse mean velocity by the turbulence models are similar to the pre-

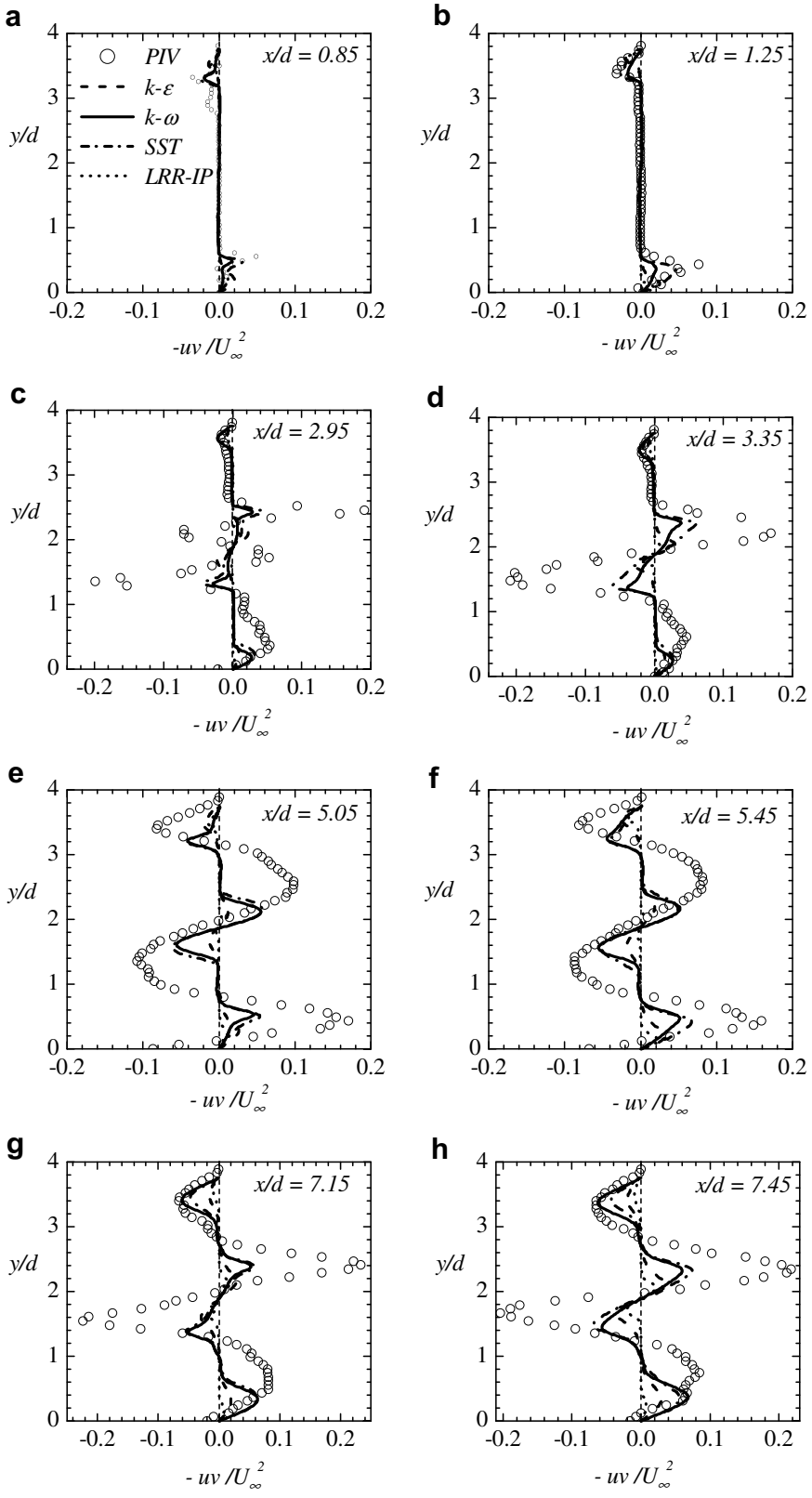

Fig. 13. Comparison between profiles of the predicted Reynolds shear stress obtained with measured values at selected x/d locations.

dictions of the streamwise component of the mean velocity.

4.2. Reynolds stresses

Unlike the LRR-IP model, the k–ε, k–ω and SST models do not calculate the individual components of the Reynolds stresses. In the case of the latter models, an assumption of isotropy was applied to estimate the Reynolds normal stresses from k as follows: $u^2 = v^2 = 2k/3$. As discussed in Paul et al. (2007), the measured values of v^2 were found to be much higher than u^2 in most of the flow region, implying that the turbulence field is not exactly isotropic. Nonetheless, estimated values of u^2 and v^2 from the k-based models and those obtained from the LRR-IP model, which calculates these quantities from their respective transport equations, are compared with the experimental data. The Reynolds shear stresses for the two-equation models are computed using $-uv = \nu_t(\partial U/\partial y + \partial V/\partial x)$, where $\nu_t = C_\mu k^2/\varepsilon$ and constant $C_\mu = 0.09$. Figs. 11 and 12 compare predicted and measured profiles of u^2 and v^2, respectively, at various x/d locations. It is clear from these figures that all the models significantly underpredicted the measured Reynolds normal stresses. At some locations, the predicted values are an order of magnitude lower than the measured values. Although, all the predictions are far from the measured, surprisingly, the values approximated from the isotropic assumption for the k–ε, k–ω and SST models are marginally closer to the measured values than the results from LRR-IP model. This observation is consistent with the experience of Meyer (1994) and Balabani et al. (1994).

Fig. 13 compares the measured and predicted profiles of the Reynolds shear stress at selected x/d locations. The predicted results, especially those obtained from the k–ε, k–ω, and SST models, are in reasonably good agreement with the experimental data in some regions of the flow. Meyer (1994) also reported poor Reynolds stresses predictions from a second moment closure that used a wall function. As noted earlier, the LES studies by Rollet-Miet et al. (1999) and Hassan and Barsamian (2004) produced Reynolds stress values that are in good agreement with the experiment of Simonin and Barcouda (1988).

4.3. Production of turbulent kinetic energy and Reynolds stresses

For a two-dimensional turbulent flow, the production terms in u^2, v^2 and uv are:

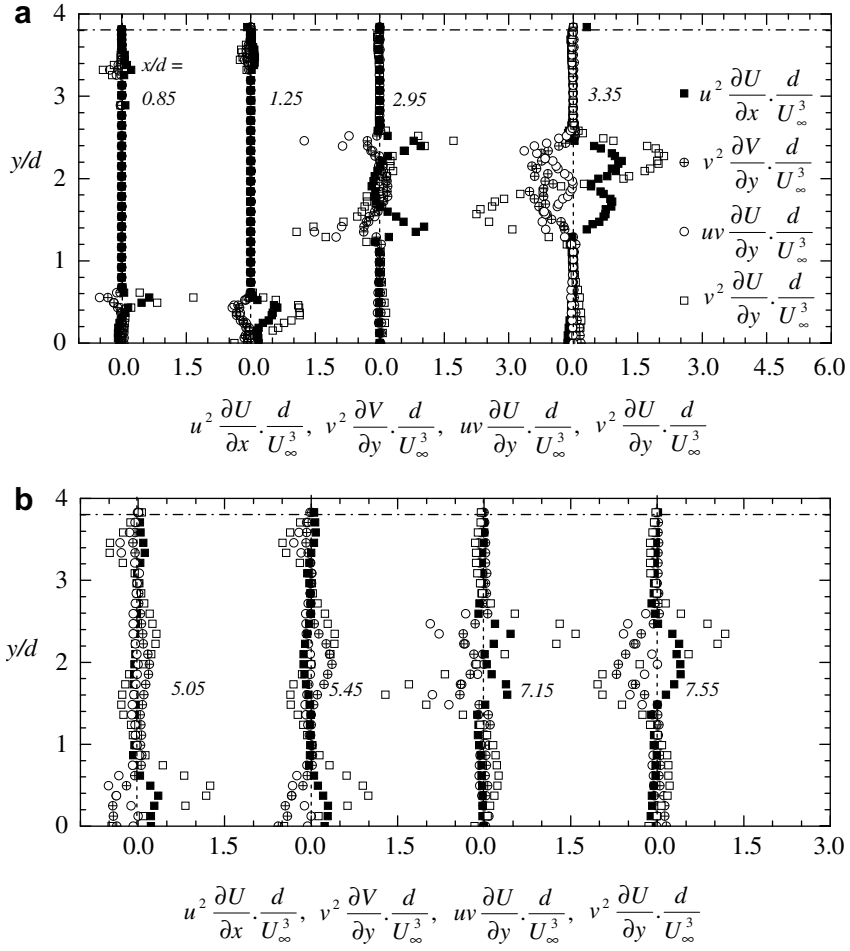

Fig. 14. Profiles of turbulence production by Reynolds stresses. Each term is non-dimensionalized by U_∞^3/d.

$$P_{uu} = -u^2\partial U/\partial x - uv\partial U/\partial y \quad (13)$$

$$P_{vv} = -v^2\partial V/\partial y - uv\partial V/\partial x \quad (14)$$

$$P_{uv} = -u^2\partial V/\partial x - v^2\partial U/\partial y \quad (15)$$

respectively. Similarly, the production term in the turbulent kinetic energy equation is

$$P_k = [P_{k,N}] + [P_{k,S}] = [-u^2\partial U/\partial x - v^2\partial V/\partial y] + [-uv(\partial U/\partial y + \partial V/\partial x)] \quad (16)$$

In classical turbulent flows such as fully developed channel and zero pressure gradient turbulent boundary layers, all the mean velocity gradients except $\partial U/\partial y$ are identically zero or negligibly small compared with $\partial U/\partial y$. If these boundary layer assumptions are invoked, $P_{uv} \approx v^2\partial U/\partial y$, $P_{uu} \approx uv\partial U/\partial y$, and $P_k \approx uv\partial U/\partial y$. In this case $P_{uu} = P_k$ while P_{vv} becomes negligibly small. As shown and discussed in Paul et al. (2007), all the four velocity gradients are significant in most regions of this tube bundle cross-flow. In this section, the implications of this observation to the measured production of Reynolds stresses and turbulent kinetic energy in tube bundles are discussed. Finally, the measured values are compared with predicted values.

The distributions of $u^2\partial U/\partial x$, $v^2\partial V/\partial y$, $uv\partial U/\partial y$ and $v^2\partial U/\partial y$ based on measurement are shown in Fig. 14. Each of these terms is extremely high in the recirculation region where the shear layer is the largest. It appears that the bulk of turbulence is produced in the recirculation region and transported towards the minimum flow cross-sectional area. The term $v^2\partial U/\partial y$ is certainly the largest, and explains the very high levels of $-uv$ reported earlier. In contrast to classical turbulent boundary layers, the terms $u^2\partial U/\partial x$ and $v^2\partial V/\partial y$ are not negligible compared to $uv\partial U/\partial y$. In most regions of the flow, the magnitude of $u^2\partial U/\partial x$ and $v^2\partial V/\partial y$ are nearly similar or higher than $uv\partial U/\partial y$. Therefore, the dynamic importance of $u^2\partial U/\partial x$ and $v^2\partial V/\partial y$ cannot be neglected in turbulent flow in a tube bundle. It is also important to observe that the magnitude of $v^2\partial V/\partial y$ exceeds that of $(u^2\partial U/\partial x + uv\partial U/\partial y)$. This implies that the production term in v^2 exceeds that in u^2, and explains the relatively higher values of v^2 than u^2. This is also at variance with simple turbulent flows where u^2 is typically higher than v^2 because energy from the mean flow is transferred to u^2 and then redistributed to v^2.

The profiles of the total production term, P_k, as well as the contributions of the normal, $P_{k,N}$, and shear, $P_{k,S}$, components as indicated in Eq. (16) are shown in Fig. 15. The figure reveals that although $u^2\partial U/\partial x$ and $v^2\partial U/\partial y$ are individually high (Fig. 14), their sum is smaller because they are of opposite sign. Although $P_{k,S}$ exceeds $P_{k,N}$ in most

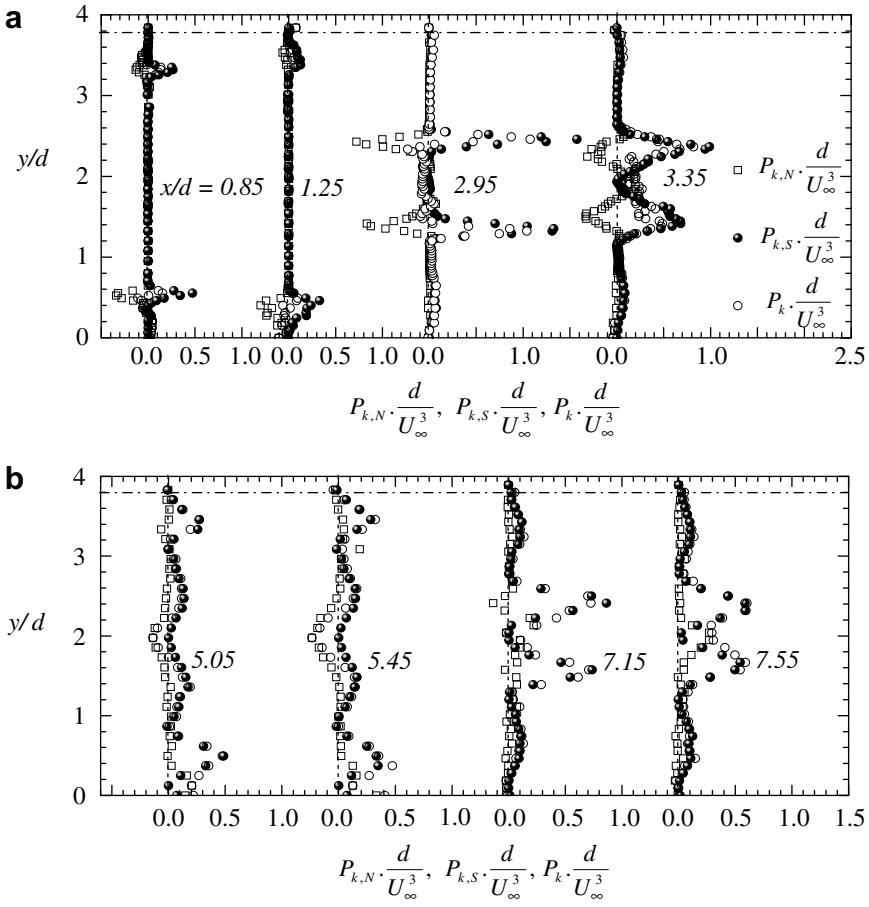

Fig. 15. Profiles of turbulence production by turbulent kinetic energy. Each term is non-dimensionalized by U_∞^3/d.

of the flow domain, the contribution of $P_{k,N}$ is not negligible. In fact, in some local regions within the recirculation zone (e.g. $y/d = 1.5$–2.5 at $x/d = 5.05$ and 5.45), $P_{k,N} > P_{k,S}$ and the total production, P_k becomes negative. The profiles of the total production P_k at $x/d = 0.85$ and 1.25 show double peak values of approximately -0.1 and 0.1 in the

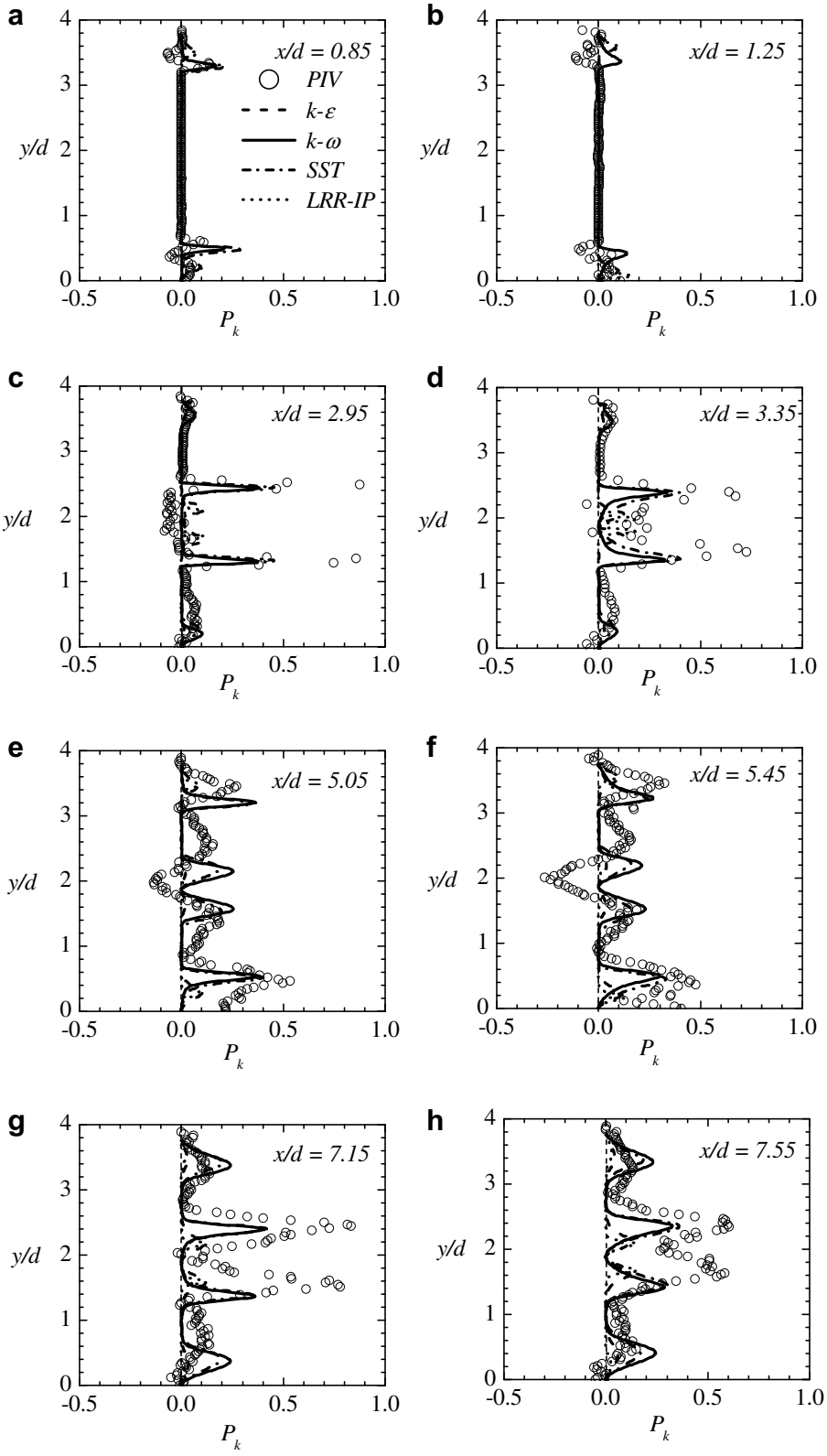

Fig. 16. Comparison between the predicted and measured values of the total turbulence production by turbulent kinetic energy at selected x/d locations. The term is normalized by U_∞^3/d.

recirculation zones. The changes in signs of the peak values are due to two vortices, similar in size, nearly symmetrical about the tube's horizontal center line, and opposite in rotational direction, that were formed at these x/d locations. These peak values are lower in magnitude than those at other x/d locations. It is also observed that in the region

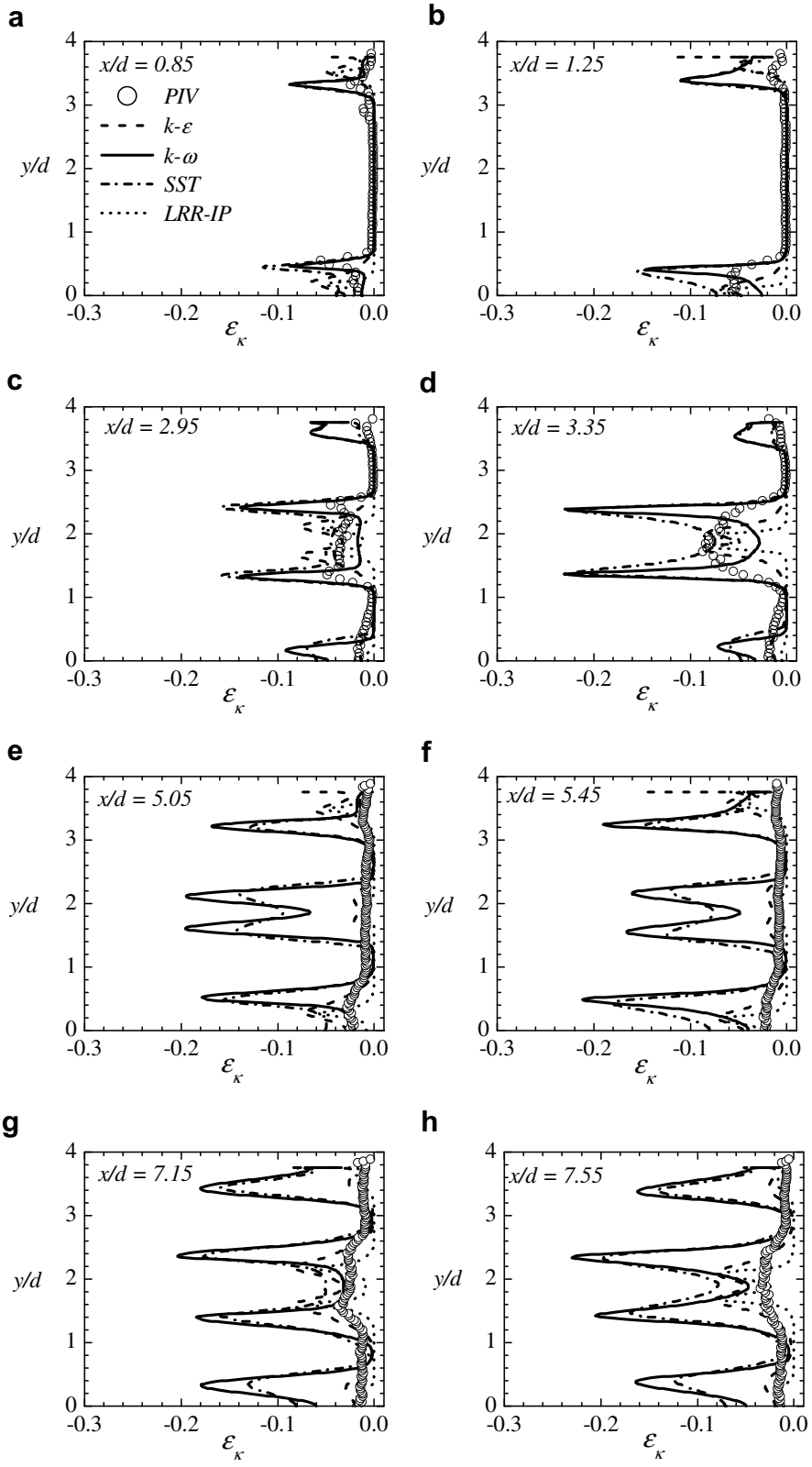

Fig. 17. Comparison between the predicted dissipation rate with measured values at selected x/d locations. The term is normalized by U_∞^3/d.

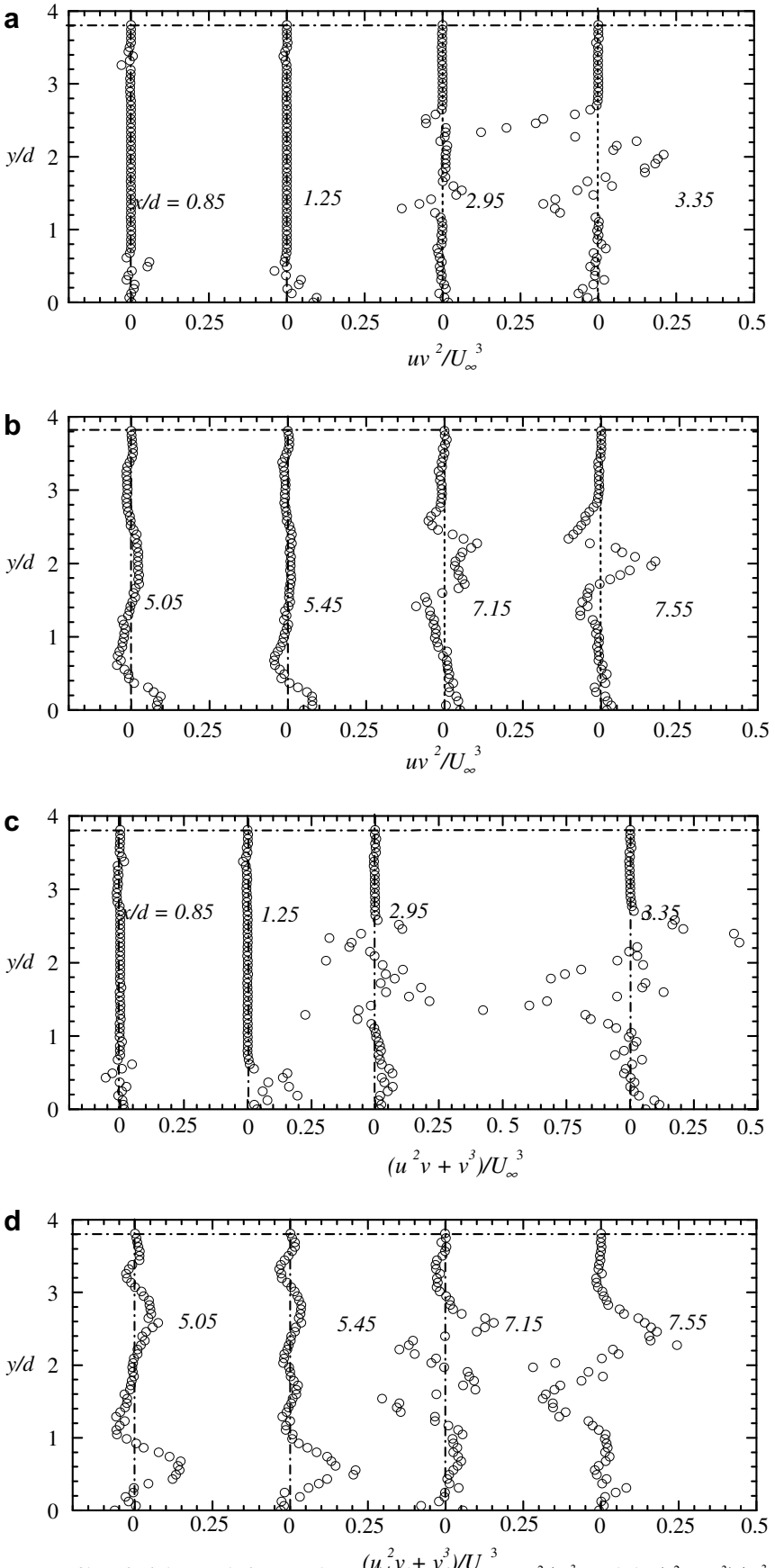

Fig. 18. Profiles of triple correlation at selected x/d locations: (a) uv^2/U_∞^3 and (b) $(u^2v + v^3)/U_\infty^3$.

where the flow becomes spatially periodic (i.e., $x/d \geqslant 5.05$), the profiles of P_k have double positive peaks, one in the recirculation zone and the other in the passage between rows of tubes. However, at each x/d location, the peak in the recirculation zone is relatively higher than the corresponding one in the passage between the rows of tubes. Figs. 14 and 15 clearly demonstrate some important differences between turbulence production mechanisms in tube bundles and those observed in simple turbulent boundary layers. These differences may partly explain the inability of standard k–ε and k–ω models to accurately predict turbulent flows in tube bundles.

Fig. 16 compares the measured and predicted profiles of the production term in the turbulent kinetic energy equation at selected x/d locations. In general, the turbulence models predict the trend and peak value at all x/d locations reasonably well. Although most of the models fail to predict the exact level of P_k at all y/d locations, all of them correctly predict the locations of the higher peaks at most of the x/d locations. None of the models was able to reproduce the negative production measured at $x/d = 5.05$ and 5.45. However, the ε-based models provide better prediction in value and trend.

Fig. 17 shows that the dissipation rate profiles, based on the measured values, reach maxima in the recirculation regions (where production was also found to be maximum) and are often much smaller in magnitude outside these regions. It is also observed from these profiles that the dissipation rate rises from the recirculation region of the first row to a maximum value in the recirculation region at $x/d = 3.35$ (Fig. 17d). This significant increase is not found in the spatially periodic region (i.e., $x/d \geqslant 5.05$). All the models predicted higher values than measured. The huge differences between the predicted and measured values are partly due to the inability of the PIV to resolve the small scales which led to an underestimation of the dissipation rate. It should be noted that agreement between the experimental data and predictions is better in the developing region ($x/d = 0.85$–3.35) than in the spatially periodic region ($x/d = 5.05$–7.55). Although the LRR-IP model results agree best with measured data, it is not possible to conclude that LRR-IP model performs better because the measured values are likely underestimated.

5. Triple velocity correlations and convection term of turbulent kinetic energy

The following four triple correlations were measured: u^3, uv^2, u^2v, v^3. The term u^3 represents the transport of u^2 in the streamwise direction while uv^2 represents the transport of the uv in the transverse direction. Similarly, u^2v and v^3 are associated with the transport of u^2 and v^2, respectively,

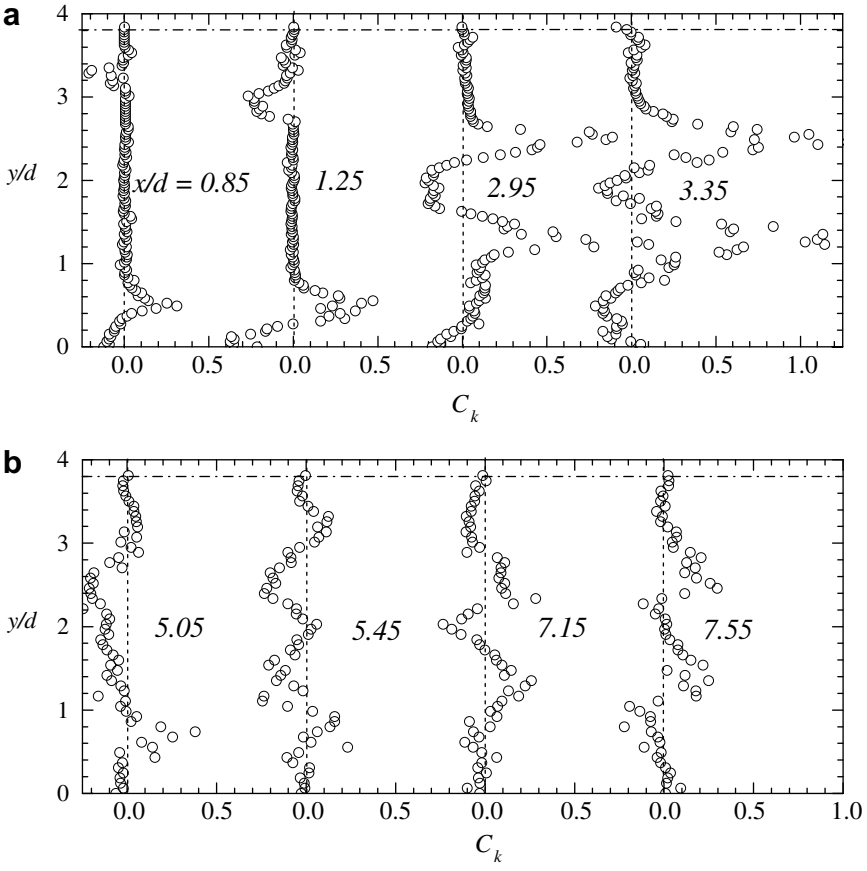

Fig. 19. Profiles of convection term in the turbulent kinetic energy budget at selected x/d locations. The term is normalized by U_∞^3/d.

in the transverse direction. Their gradients, which represent turbulence diffusion in the transport equations for the turbulent kinetic energy and Reynolds stresses, were evaluated but they showed significant scatter. It was therefore decided to present only the triple products instead. The quantity u^3 also showed considerable scatter and is, therefore, not reported. The term uv^2 is shown in Fig. 18a and b. The gradient $\partial uv^2/\partial y$ is associated with the diffusion of $-uv$. The sum $u^2v + v^3$ is plotted in Fig. 18c and d. Since the gradient $[\partial(u^2v + v^3)/\partial y]$ is associated with the diffusion of turbulent kinetic energy in the transverse direction, plotting the sum $u^2v + v^3$ is more meaningful than plotting the individual terms, u^2v and v^3. Fig. 18a and b show that profiles of uv^2 have peak values in the recirculation regions but become negligible at the minimum flow cross-sectional areas. This implies that most of the Reynolds shear stress is produced in the recirculation region and diffused into the minimum cross-sectional areas. Similarly, there is a significant diffusion of turbulent kinetic energy from the recirculation region (where most of the energy is produced) into the minimum cross-sectional areas.

The convection of turbulent kinetic energy by the mean flow was estimated from Eq. (4). This convection term, normalized by U_∞^3/d, is plotted in Fig. 19 at various x/d locations. The x-axis range for the repeated sections in the figure is 0.0–1.0. It is observed that the peak values of C_k have their largest values at $x/d = 3.35$. These maxima occur in the wake regions. This significant increase was not found downstream of the third and subsequent rows. Moreover, the convection term as shown in the figure is predominantly positive at all x/d locations. It is expected, therefore, that the convection input of energy appears as a positive contribution in the energy balance at most of the locations.

6. Conclusions

The results of the present experimental and numerical studies of turbulent cross-flow in a staggered tube bundle yield the following conclusions:

1. The experimental results reveal that the transverse turbulent intensity is significantly higher than the streamwise turbulent intensity. The contribution of the normal stresses to the production of turbulent kinetic energy is similar or larger than the shear component in most regions of the flow. As a result, the net production becomes negative in some regions of the tube bundle flow. The levels of turbulence diffusion and convection terms in the transport equation for the turbulent kinetic energy are significant, so that the production of turbulent kinetic energy and its dissipation rate are not in equilibrium, as assumed in many basic eddy viscosity turbulence models.
2. In spite of these features of turbulent flow in staggered tube bundles, it was observed that the overall performance of the k-based two-equation models appears closer to the measured data than that of the particular second moment closure (LRR-IP) used in this study. For example, the Reynolds normal stresses obtained from the k-based models are in better agreement with measured values than those obtained from the second moment closure model. This might be due to the steady form used in this work. Comparisons between the numerical and measured values demonstrate that the mean velocity profiles were reasonably well predicted by all the turbulence models. In the tube wake, however, the LRR-IP model gave better results for the mean velocity than the other models. At the impact region, the k–ε model predictions of the mean velocity profiles were seen to be in excellent agreement with the measured values.
3. For the mesh distributions used in the present work, the k–ε and LRR-IP models showed less sensitivity to changes in the grid resolution than k–ω and SST. A refinement of the mesh in all areas of the flow (not just in regions near walls) that may be necessary to overcome this sensitivity, however, would lead to a significant number of nodes in an x–y plane. This refinement would lead to very large numbers of nodes for a 3D computation. Even in the present work, the computational effort required for cases using Grid D was significant; due to the requirement of three nodes in the z-direction, three identical z-planes were computed with a total number of nodes greater than 1.4 million.

Acknowledgement

The financial support of the Natural Sciences and Engineering Research Council of Canada (NSERC) and the Canada Foundation for Innovation (CFI) is gratefully acknowledged.

References

Balabani, S., 1996. An experimental investigation of the cross-flow over tube bundles, Ph.D. thesis, King's College, London.

Balabani, S., Bergeles, G., Burry, D., Yianneskis, M., 1994. Velocity characteristics of the cross-flow over tube bundles. In: International Proceedings of the 7th International Symposium on Application of Laser Anemometry to Fluid Mechanics, Lisbon, vol. 2, pp. 39.3.1–39.3.8.

Barth, T.J., Jesperson, D.C., 1989. The design and application of upwind schemes on unstructured meshes. In: AIAA 27th Aerospace Sciences Meeting, AIAA 89-0366.

Benhamadouche, S., Laurence, D., 2003. LES, coarse LES, and transient RANS comparisons on the flow across a tube bundle. Int. J. Heat Fluid Flow 24, 470–479.

Bouris, D., Bergeles, G., 1999. Two dimensional time dependent simulation of the subcritical flow in a staggered tube bundle using a subgrid scale model. Int. J. Heat Fluid Flow 20, 105–114.

Fouras, A., Soria, J., 1998. Accuracy of out-of-plane vorticity measurements derived from in-plane velocity field. Exp. Fluids 25, 409–430.

Gatski, T.B., Rumsey, C.L., 2002. Linear and nonlinear eddy viscosity models. In: Launder, Brian, Sandham, Neil (Eds.), Closure Strategies for Turbulent and Transitional Flows. Cambridge University Press, pp. 10–46.

Grotjans, H., Menter, F.R., 1998. Wall functions for general application CFD codes, ECCOMAS 98. In: Proceedings of the Fourth European Computation Fluid Dynamics Conference, pp. 1112–1117.

Hanjalic, K., 1994. Advanced turbulent closure models: a view of current status and future prospects. Int. J. Heat Fluid Flow 15 (3), 178–203.

Hassan, Y.A., Barsamian, H.R., 2004. Tube bundle flows with the large eddy simulation technique in curvilinear coordinates. Int. J. Heat Mass Transfer 47, 3057–3071.

Hwang, R.R., Jaw, S.Y., 1998. Second-order closure turbulence models: their achievements and limitations. Proc. Natl. Sci. Council ROC (A) 22 (6), 703–722.

Hinze, J.O., 1975. Turbulence. McGraw-Hill, New York.

Launder, B.E., Spalding, D.B., 1994. The numerical computation of turbulent flows. Comput. Methods Appl. Mech. Eng. 3, 269–289.

Launder, B.E., Reece, G.J., Rodi, W., 1975. Progress in the development of a Reynolds stress turbulence closure. J. Fluid Mech. 68, 537–566.

Lecordier, B., Demare, D., Vervisch, L.M.J., Reveillion, J., Trinite, M., 2001. Estimation of the accuracy of PIV treatments for turbulent flow studies by direct numerical simulation of multi-phase flow. Meas. Sci. Technol. 12, 1382–1391.

Leschziner, M.A., Launder, B.E., 1993. Round normally impinging turbulent jet and turbulent flow through tube bank sub-channel. In: Proceedings of the second ERCOFTAC-IAHR Workshop on Refined Flow Modelling, UMIST, UK.

Leschziner, M.A., 2006. Modelling turbulent separated flow in the context of aerodynamic applications. Fluid Dyn. Res. 38, 174–210.

Menter, F.R., 1994. Two-equation eddy-viscosity turbulence models for engineering applications. AIAA J. 32 (8), 37–40.

Meyer, K.E., 1994. Experimental and numerical investigation of turbulent flow and heat transfer in staggered tube Bundles. Ph.D. thesis, Technical University of Denmark.

Moulinec, C., Pourquie, M.J.B.M., Boersma, B.J., Nieuwstadt, F.T.M., 2004. Direct numerical simulations on a Cartesian mesh of the flow through a tube bundle. Int. J. Comput. Fluid Dyn. 18 (1), 1–14.

Patankar, S.V., 1980. Numerical Heat Transfer and Fluid Flow, Hemisphere. Hemisphere Publishing Corporation, New York.

Paul, S.S., Ormiston, S.J., Tachie, M.F., 2004. Analysis of turbulent flow in staggered tube bundles. In: Proceedings of the 12th Annual Conference of the CFD Society of Canada, Heat Transfer 1, Ottawa, Canada, pp. 239–246.

Paul, S.S., Tachie, M.F., Ormiston, S.J., 2007. Experimental study of turbulent cross-flow in a staggered tube bundle using particle image velocimetry. Int. J. Heat Fluid Flow 28, 441–453.

Piirto, M., Saarenrinne, P., Eloranta, H., Karvinen, R., 2003. Measuring turbulence energy with PIV in a backward-facing step flow. Exp. Fluids 35, 219–236.

Pope, S.B., 2000. Turbulent Flows. Cambridge University Press, UK.

Rhie, C.M., Chow, W.L., 1983. A numerical study of the turbulent flow past an isolated airfoil with trailing edge separation. AIAA J. 21 (11), 1521–1532.

Rollet-Miet, P., Laurence, D., Ferziger, J., 1999. LES and RANS of turbulent flow in tube bundles. Int. J. Heat Fluid Flow 20, 241–254.

Saarenrinne, P., Piirto, M., 2000. Turbulent kinetic energy dissipation rate estimation from PIV velocity vector fields. Exp. Fluids, S300–S307.

Simonin, O., Barcouda, M., 1988. Measurement and prediction of turbulent flow entering a staggered tube bundle. In: Proceedings of the 4th International Symposium on Applications of Laser Anemometry to Fluid Mechanics, Lisbon, Portugal.

Watterson, J.K., Dawes, W.N., Savill, A.M., White, A.J., 1999. Predicting turbulent flow in a staggered tube bundle. Int. J. Heat Fluid Flow 20, 581–591.

Wilcox, D.C., 1988. Multiscale model for turbulent flows. AIAA J. 26, 1311–1320.